Journal of Manufacturing Processes 154 (2025) 311–331

Contents lists available at ScienceDirect

Journal of Manufacturing Processes

journal homepage: www.elsevier.com/locate/manpro

Failure behavior prediction for resistance spot-welded three-layered dissimilar joints with advanced high-strength steel

Viktoria Olfert [a], Philipp Bähr [b], Lilia Schuster [c], Julia Westhoff [d], Keke Yang [a,*], Enes Ibeski [a], David Hein [a], Silke Sommer [b], Gerson Meschut [a]

[a] Laboratory for Material and Joining Technology (LWF), 33098, Paderborn, Germany
[b] Fraunhofer Institute for Mechanics of Materials (IWM), Wöhlerstrasse 11, 79108, Freiburg, Germany
[c] Karlsruhe Institute of Technology (KIT), wbk Institute of Production Science, Kaiserstr. 12, 76131, Karlsruhe, Germany
[d] divis intelligent solutions GmbH, Joseph-von-Fraunhofer-Straße 20, 44227, Dortmund, Germany

ARTICLE INFO

Keywords:
Resistance spot welding
Multi-layered joint
Load-bearing capacity
Failure behavior
Ultra-high-strength steel

ABSTRACT

Multi-layered sheet joints featuring both material and thickness dissimilarities offer a promising solution for lightweight body structures by reducing the number of spot welds and enabling a material-specific distribution of mechanical loads. However, the inherent complexity of the stack-up, along with the resulting changes in the welding process, poses significant challenges for accurately predicting the failure behavior of such joints. Consequently, a reliable and universally applicable prediction method is still lacking. To address these challenges, this study employs a comprehensive methodology that combines experimental investigations, numerical simulations, and analytical modeling. The failure behavior of nineteen distinct joint configurations was characterized under three representative loading modes, including cross-tension, tensile-shear, and tensile-peel. Building on these results, a novel analytical method was developed to enable the reliable prediction of the failure behavior of dissimilar three-layer resistance spot-welded joints. The proposed model demonstrated high predictive accuracy, achieving a coefficient of determination of 88.8 % under shear loading, 78.6 % under tensile loading, and 72.0 % under peel loading. The corresponding RMSE values ranged from 0.36 kN to 1.94 kN across all failure modes. These results confirm the model's robustness and applicability to multi-material, multi-thickness spot-welded joints. Based on these findings, the developed method serves as an efficient and reliable tool for evaluating the quality and safety of multi-layered spot-welded joints in lightweight thin-walled structures.

1. Introduction

Climate change, the increasingly limited availability of resources, and the resulting political directives for greenhouse gas reduction pose significant challenges to the automotive industry [1]. In response, lightweight construction has emerged as a key strategy for meeting climate targets. In recent years, a variety of approaches for reducing vehicle weight have been proposed [2]. Among them, the use of high-strength steels has shown particularly high potential, as it allows for substantial weight savings without compromising crash safety, structural integrity, or energy efficiency [3]. Specifically, press-hardened steel (PHS) and advanced high-strength steel (AHSS) have become widely adopted in the structural reinforcement components of vehicle safety cages [4], due to their favorable strength-to-weight ratios and excellent crash performance [5]. To realize the lightweight potential of these materials, suitable joining techniques are required to integrate them efficiently into vehicle body structures. Among the available joining processes, resistance spot welding (RSW) has emerged as the predominant technique for high-strength steels in body-in-white (BIW) assembly, due to its compatibility with large-scale production requirements [6].

In addition to lightweight design, recent global crises and increasingly volatile markets have shifted the automotive industry's focus toward energy and production efficiency [7]. In this context, multi-sheet joints offer a promising solution by reducing the number of spot welds, thereby improving energy efficiency and enabling a material-specific

* Corresponding author.
E-mail address: keke.yang@lwf.uni-paderborn.de (K. Yang).

https://doi.org/10.1016/j.jmapro.2025.09.077
Received 13 August 2025; Received in revised form 24 September 2025; Accepted 28 September 2025
Available online 6 October 2025

distribution of mechanical loads [8]. Compared to two-layered joints (2-LJ), using three-layered joints (3-LJ) can reduce the number of welds needed in the BIW assembly by about 30 % [9]. However, these advantages are accompanied by a substantial increase in process complexity. In particular, the presence of dissimilar and thickness-varied sheet stack-ups complicates current flow and heat distribution during welding, leading to increased variability in nugget formation [10]. As a result, the accurate prediction of joint load-bearing capacity remains both technically challenging and essential for structural safety [11]. Given that a modern steel car body typically comprises 4.000 to 6.000 spot welds - accounting for approximately 80 % of the total welding workload [12] - ensuring weld quality at such scale becomes increasingly challenging. Consequently, developing an accurate method to predict the load-bearing capacity of spot welds is essential to ensure structural reliability and support efficient vehicle design.

To address this need, a wide range of studies and predictive models are currently available for 2-LJ. Chebbi et al. [13] investigated the influence of welding parameters on the mechanical behavior of spot welds of 2-LJ under tensile and peel loading conditions. Their results highlight the strong influence of welding parameters on joint mechanical behavior, underscoring their importance as key variables in predictive modeling. Subsequently, Boriwal et al. [14] and Rajalingam et al. [15] developed mathematical models to predict the load-bearing capacity based on welding current, welding time, and electrode force. However, the predictive accuracy of these parameter-based models is limited, as they require recalibration for each specific material combination. Other approaches describe load-bearing capacity based on key joint characteristics. Vijayan et al. [16] demonstrated a linear relationship between nugget diameter and tensile strength for 2-LJ made of dual-phase steel. Similarly, Dorribo [17] identified a linear correlation between shear tensile strength and nugget diameter in 2-LJ using press-hardened steel (PHS). This relationship was further validated for 3-LJ configurations by Pouranvari and Marashi [18], confirming its general applicability across different stack types. However, the influence of nugget diameter on the load-bearing capacity under cross-tension loading is not consistent across all materials. In the case of PHS, for example, increasing the nugget size does not lead to a significant improvement in load-bearing capacity under cross-tension loads [19]. Moreover, the effect of nugget diameter should not be considered in isolation. It interacts with other factors such as sheet thickness, tensile strength, and joint stiffness, all of which must be jointly considered in the development of accurate predictive models.

Furthermore, Cho et al. [20] demonstrated that the tensile strength of the base material significantly influences the load-bearing capacity of spot-welded joints. Specifically, the lower the tensile strength of the materials, the smaller the effect of nugget diameter on the joint's shear tensile strength. In addition, the load-bearing capacity under shear tensile loading tends to plateau once the strength limit of the weaker sheet is reached. When the failure mode shifts to base material fracture or tear-out fracture, further enlargement of the nugget no longer increases the joint strength [21]. These findings support the application of the minimum principle, which states that the load-bearing capacity of dissimilar welds can be estimated by treating the weaker partner as a similar joint. Unlike similar joints, where both joining partners share the same thickness and strength, dissimilar joints combine sheets with differing properties such as ultimate tensile strength, uniform elongation, and sheet thickness. However, although the minimum principle reliably predicts the failure location, it does not fully capture the influence of the weaker joining partner on overall joint strength. The stiffness and deformation behavior of the weaker sheet can affect the effective load distribution, thereby limiting the accuracy of simplified predictive models [22]. To address this issue, Varbai et al. [23] proposed an equation-based approach derived from the American AWS D8.1M [24] standard, incorporating sheet thickness and tensile strength of the sheet steel. However, as sheet tensile strength increases, the model tends to underestimate the load-bearing capacity. To overcome this limitation, Májlinger et al. [25] developed an alternative equation aimed at maintaining a constant deviation between the measured and predicted shear tensile strength, thereby extending its applicability to higher-strength steels. Nevertheless, both approaches predict only the minimum load-bearing capacity and do not account for the influence of nugget diameter.

While the load-bearing behavior of 2-LJ has been widely investigated, research on 3-LJ remains limited and is often restricted to specific influencing factors rather than the development of comprehensive predictive frameworks. Pouranvari and Marashi [26] experimentally demonstrated that the nugget diameter required to induce a transition from interfacial fracture to button pull-out fracture in 3-LJ depends on the applied loading method. In this context, the nugget diameter refers to the effective diameter between the respective tensioned sheet interfaces. Another defining characteristic of multi-layered spot-welded joints is the variation in stacking sequence, as individual sheets can be arranged in different orders. Mao et al. [27] found that different sequences significantly affect the mechanical properties of 3-LJ. This effect is primarily attributed to the fact that changes in stacking sequence alter the heat flow during welding, which in turn affects the nugget geometry and microstructural characteristics.

The above analysis of the current state of the art reveals that, while the failure behavior of 2-LJ has been widely investigated, the failure mechanisms of 3-LJ remain insufficiently investigated and lack a systematic study. Compared to 2-LJ, 3-LJ exhibit increased structural complexity, which substantially modifies key influencing factors, such as nugget geometry, that govern failure modes. As a result, 3-LJ may demonstrate fundamentally different failure behaviors. Consequently, the applicability of existing failure prediction models developed for 2-LJ to 3-LJ remains uncertain and demands systematic investigation. Given the growing use of dissimilar 3-LJ in vehicle body structures, a comprehensive understanding and reliable prediction of their failure behavior is gaining increasing attention due to its practical significance in automotive safety.

Numerical simulation is increasingly employed to reduce the need for extensive experimental testing and to improve the efficiency of welding process design. Considerable efforts have been made to predict the deformation and failure behavior of RSW using finite element analysis (FEA). Mikno et al. [28] investigated the shear force generated during static tensile tests of RSW joints using 3D FEM, while Nielsen [29] applied an elastic–viscoplastic constitutive model (Gurson) to study ductile plug failure under shear loading. Chung et al. [30] conducted a full 3D FEM of RSW under lap-shear and U-shape tension loads and demonstrated that reliable failure predictions can be achieved even when only the base material and fusion zone are considered, without distinguishing the HAZ. Sadasue et al. [31] extended this approach by assigning distinct constitutive properties to the FZ, HAZ, and BM, thereby improving the accuracy of failure predictions in high-strength steels. Recent work has demonstrated that reliable prediction of RSW failure requires zone-resolved characterization of nugget, HAZ, and base material, as local constitutive and fracture properties deviate markedly from the parent sheet and govern mode transitions [32]. More recently, refined approaches such as the equivalent displacement method (EDM) have been proposed to further enhance the accuracy of FEM predictions for tensile-shear loading [33]. These studies underline the effectiveness of advanced FEM in predicting deformation behavior and failure modes of RSW joints, while also highlighting the challenges posed by the complex metallurgical heterogeneity of nugget and HAZ. Complementing empirical approaches, recent multi-physical FE frameworks couple electro-thermal-mechanical fields for RSW, enabling more faithful linkages between welding schedules, nugget growth, and subsequent joint response under mechanical loading [34].

For multilayer joints, simplified surrogate models have been developed to enable efficient crash simulations. Chtourou et al. [35] proposed a connector-based formulation for 3-BV, calibrated and validated under multiple loading orientations, which reproduced experimental force-

displacement curves with good accuracy. However, the approach neglected bending terms in the failure criterion and was validated only for nearly symmetric joints. Khan et al. [36] applied the MAT_100_DA model in LS-DYNA for both 2-BV and 3-BV, with parameter optimization using LS-OPT. Two modeling approaches were compared: independent representations of each 2-BV and an integrated "weld assembly" model. While both approaches matched experimental load-displacement curves, the independent method was favored, as it more accurately reproduced failure confined to the loaded interface. To date, most 3-BV simulations are therefore treated as two independent 2-BV, without explicitly accounting for the interactions between the two faying interfaces or the influence of the third sheet. This limitation underscores the need for more generalizable approaches to simulate the load-bearing capacity and failure mechanisms of three-layer RSW joints. In parallel, physics-informed machine learning has emerged as a complementary direction for RSW quality assessment, embedding welding physics into data-driven models to enhance generalizability and robustness [37].

Against this background, the present study experimentally investigated the load-bearing capacity and failure behavior of 2-LJ and 3-LJ across nineteen different joint configurations, intending to systematically identify the correlation between load-bearing capacity and various influencing factors. These factors include the loading mode (cross-tension, tensile-shear, and tensile-peel), stacking sequence, sheet thickness, ultimate tensile strength, load introduction method, material combination, and joint-specific characteristics. To further deepen the understanding of the underlying failure mechanisms, numerical simulations were conducted in parallel with the experiments, enabling a detailed analysis of the stress and deformation behavior of 3-LJ. Based on the combined experimental and numerical results, the feasibility of transferring the analytical approach developed for 2-LJ to 3-LJ was systematically evaluated. A predictive method for predicting the failure behavior of 3-LJ, including load-bearing capacity and failure modes, was developed. This method is based on statistical analysis and incorporates physics-informed input parameter selection to ensure generalizability and transferability across different joint configurations. This approach ensures that only variables with a direct physical correlation to joint load-bearing capacity, such as nugget diameter, sheet thickness, tensile strength, and stiffness-related parameters, are included in the predictive framework. By integrating physically interpretable variables into the model-building process, the methodology enhances predictive accuracy while maintaining transferability across different material combinations and loading paths. This physics-informed strategy represents a novel contribution of the present study, distinguishing it from existing empirical regression models and supporting the development of a universally applicable prediction method for multi-layer spot welds.

The results of this study systematically reveal the failure characteristics of three-layer resistance spot-welded joints, providing a theoretical basis for predicting their failure behavior.

2. Experimental setup and details

2.1. Materials

The materials used in this study included zinc-coated HC340LA steel sheets with thicknesses of 0.8 mm and 1.2 mm, zinc-coated HCT590X steel with a thickness of 1.5 mm, zinc-coated HCT780X steel with a thickness of 1.0 mm, and aluminum-silicon-coated press-hardened steel CR1900T with a thickness of 1.0 mm. The mechanical properties of the base material were determined by uniaxial tensile tests conducted on a universal testing machine at a constant crosshead speed of 10 mm/min. The material properties of the steels, including ultimate tensile strength (UTS), yield strength (YS), total elongation (TE), and hardness HV0.1, are presented in Table 1.

To determine the shape and microstructure of the weld nugget, cross-sections of the spot welds were prepared for metallographic examination. The specimens were etched with a 4 % nital solution to facilitate the microstructure evaluation and expose the geometry of the weld nugget observed under a metallographic microscope. Distinct regions within the spot weld, specifically the fusion zone (FZ) of the weld nugget, the heat-affected zone (HAZ), and the base material (BM) were identified.

Table 1
Mechanical properties of the utilized material combination determined by tensile test.

	0.2 % Yield Strength $R_{p0.2}$ in MPa	Tensile Strength R_m min. in MPa	Total elongation A_{80} min. in %	Hardness $HV_{0.1}$
HC340LA	437	466	37	135
HCT590X	396	663	31	200
HCT780X	671	872	22	252
CR1900T	1342	2010	8	675

Twelve different 2-LJ and seven 3-LJ were selected to investigate the role of the third sheet in the failure behavior, including both load-bearing capacity and failure mode (Table 2). For the 2-LJ, both similar and dissimilar joints were considered. Additionally, joint configuration G was included using CR1500T as the passive outer sheet to examine the influence of the tensile strength of press-hardened steels (PHS) on the load-bearing capacity.

2.2. Resistance spot welding

Resistance spot welding was carried out using a Nimak power GUN

Table 2
Two-layered and three-layered joining configurations selected to investigate.

No.	Sheets	Anode side material	Middle layer material	Cathode side material
a	2	HC340LA $t = 0.8$ mm	–	HC340LA t = 0.8 mm
b	2	HC340LA $t = 1.2$ mm	–	HC340LA t = 1.2 mm
c	2	HCT590X t = 1.5 mm	–	HCT590X $t = 1.5$ mm
d	2	HCT780X $t = 1.0$ mm	–	HCT780X $t = 1.0$ mm
e	2	CR1900T t = 1.0 mm	–	CR1900T t = 1.0 mm
f	2	CR1900T t = 1.0 mm		HCT780X t = 1.0 mm
g	2	CR1900T t = 1.0 mm	–	HCT590X $t = 1.5$ mm
h	2	CR1900T $t = 1.0$ mm	–	HC340LA $t = 0.8$ mm
i	2	CR1900T $t = 1.0$ mm	–	HC340LA $t = 1.2$ mm
j	2	HC340LA $t = 0.8$ mm	–	HC340LA t = 1.2 mm
k	2	HC340LA t = 1.2 mm	–	HCT780X $t = 1.0$ mm
l	2	HC340LA t = 0.8 mm	–	HCT590X $t = 1.5$ mm
A	3	HC340LA $t = 0.8$ mm	CR1900T $t = 1.0$ mm	HC340LA $t = 1.2$ mm
B	3	HC340LA t = 1.2 mm	CR1900T t = 1.0 mm	HCT780X t = 1.0 mm
C	3	CR1900T t = 1.0 mm	HC340LA $t = 0.8$ mm	HCT590X $t = 1.5$ mm
D	3	CR1900T $t = 1.0$ mm	HC340LA t = 1.2 mm	HCT780X t = 1.0 mm
E	3	CR1900T t = 1.0 mm	CR1900T t = 1.0 mm	HCT590X t = 1.5 mm
F	3	HCT590X t = 1.5 mm	HC340LA t = 0.8 mm	HCT590X t = 1.5 mm
G	3	CR1500T t = 1.0 mm	HC340LA $t = 0.8$ mm	HCT590X t = 1.5 mm

2-C spot welding gun with a C-type transformer and an HWH Genius HWI436WA weld controller. A dome-shaped Cu—Cr welding electrode cap met the F1 16–20– 8 specifications in accordance with DIN EN ISO 18278-2:2016–09 [38] was used. Furthermore, electrodes were water-cooled at a rate of 4 L/min.

The size of the weld nugget was defined as the diameter of the weld at the sheet/sheet interface. The welding schedule was optimized to ensure the most possible symmetric weld nuggets without expulsion regarding the nugget diameter in both sheet/sheet interfaces.

By welding three-layered joints with three identical steel sheets, Pouranvari and Marashi [26] showed that nugget size at the sheet/sheet interface is the most important controlling factor of mechanical performance in terms of peak load and energy absorption. Therefore, the objective of this study was to produce a nugget with maximum symmetry for the three-layered joints, thereby minimizing the potential influences attributed to variations in the nugget diameter. To ensure comparability, the nugget diameter of the two-layered joints was also set to the same constant diameter, corresponding to the average optimum according to VDEh SEP1220–2 [39]:

$$d_{w,nom} = 5^{*}\sqrt{t_{min}} \quad (1)$$

Where t_{min} represents the minimum sheet thickness among the materials being welded.

The welding parameters were selected in alignment with established norms and based on literature research on the current state of research (Table 3). For the 2-LJ not containing CR1900T, the weld schedule was taken from the VDEh SEP1220–2 [39] welding standard. These joints were produced in accordance with the standard and fulfilled all requirements. However, for joints involving the press-hardened steel (PHS) CR1900T, standard welding procedures such as VDEh SEP1220 [39] are not sufficient due to the martensitic structure and limited weldability of PHS. Literature shows that long welding times promote softened heat-affected zones (SHAZ) near the nugget boundary, reducing tensile strength and increasing the risk of halo effect and dome failure [40,41]. In contrast, short welding times result in asymmetric nugget formation, especially in dissimilar joints [42]. To counteract these effects, a triple-pulse welding schedule was selected in this study, as it enables chemical homogenization and suppresses the halo effect and dome failure in CR1900T joints [41,43]. Throughout all trials, an electrode force of 3.5 kN, along with a squeeze time of 180 ms, was applied.

Table 3
Welding schedule for two-layered and three-layered joints.

No.	Pre-heating Current in kA	Pre-heating Current Time in ms	Main Welding Current in kA	Main Welding time in ms	Pulses	Cooling Time in ms
a	–	–	9	200	1	–
b	–	–	8.4	280	1	–
c	–	–	7	380	1	–
d	–	–	8.4	260	1	–
e	–	–	6.8	180	3	130
f	–	–	8.2	100	3	90
g	–	–	9.2	100	3	90
h	–	–	7.4	130	3	120
i	–	–	8.2	130	3	120
j	–	–	8.5	220	1	–
k	–	–	7.8	260	1	–
l	–	–	8.1	380	1	–
A	–	–	8.6	130	3	120
B	–	–	8.2	130	3	120
C	–	–	7.4	180	3	130
D	7.3	250	8.9	130	3	120
E	7.0	130	7.6	100	3	90
F	–	–	8.1	700	1	–
G	–	–	7.4	180	3	130

2.3. Experimental characterization of spot-welded joints

During the welding process, a HAZ develops around the FZ. The percentage of martensite present in this region influences the fracture behavior of the transformed microstructure [44]. To investigate this correlation, metallographic examinations were conducted. Specimens were prepared for microstructural and failure path observation using standard metallography procedures. The microstructure of the weld was characterized using optical microscopy (Zeiss Axio Observer 7 materials) after etching the samples with a 3 % nitric acid solution. A KB 30s Hardness tester was used to obtain the hardness mapping.

LWF-KS-2 tests (Fig. 1) were performed for all the joint configurations to evaluate the force-displacement behavior of the welds. The LWF-KS-2-specimen consists of two U-shaped specimen halves joined at the center point between the coupons [45]. Compared to the standard shear and cross-tensile tests, the LWF-KS-2-testing device provides rigidity, reducing specimen deformation. Additionally, due to its geometry, the LWF-KS-2-specimen can be loaded in different orientations. The loading orientation (θ) is defined as the orientation between the load introduction line and the line along the interface between the two coupons. Experiments were conducted in four different loading orientations (θ = 0°, 30°, 60°, 90°) and peel-load. The loading orientations 0° and 30° are referred to as shear-dominated loading orientations, and the loading orientations 60° and 90° are referred to as tensile-dominated loading orientations.

In contrast to 2-LJ, 3-LJ allow different load introduction strategies. The external load can be applied through two of the three sheets, while the third sheet remains unloaded. This unloaded sheet is referred to as a passive patch. Fig. 1 presents a schematic representation of the possible load introduction configurations, along with an example of a specimen geometry for the three-layered joint. Based on the specific combination of load-introducing sheets, the configurations are referred to as Top-Middle, Top-Bottom, and Middle-Bottom.

The fixture for testing the LWF-KS-2 specimen is bolted to two adapters. The custom fixture assembly was mounted on a Zwick 1484 universal testing machine equipped with a 200 kN load cell, operating at a constant tensile speed of 10 mm/min under room temperature conditions. Specimen deformation under all loading orientations was recorded using a three-dimensional digital image correlation (3D-DIC) system (GOM Aramis 3D). The system employs two cameras to capture stereo images, enabling precise measurement of displacement in three directions. A stochastic black–white speckle pattern was applied to the specimen surface to allow high-resolution tracking of local displacements. Calibration was performed using a certified two-step procedure with a reference target, ensuring measurement accuracy across the entire field of view. To validate the reliability of the displacement data, rigid-body motion tests were carried out, confirming that the measurement error remained within ±0.01 mm. Measurement errors were minimized by calculating displacement as the relative motion between different parts of the specimen, while movements of fixed components were excluded from the analysis. Fig. 2 shows the LWF-KS-2 specimen in its initial position, with the green arrow indicating the positions of the measurement points.

Mechanical performance was evaluated in terms of peak load, defined as the average maximum load obtained from five replicate tests. The load-displacement curves showed a peak load and maximum energy absorption at failure. The failure mode was identified by examining the fracture surfaces of the welded joints after the tensile tests.

In addition to mechanical testing, microstructural examinations and hardness mappings were conducted to characterize local variations in material properties across the weld. These investigations provide essential complementary information to the LWF-KS-2 tests: while the mechanical tests reveal the global load-displacement behavior and fracture patterns, the hardness and microstructural analyses enable identification of the local strength gradients and transformation zones that govern crack initiation and propagation. This combined approach

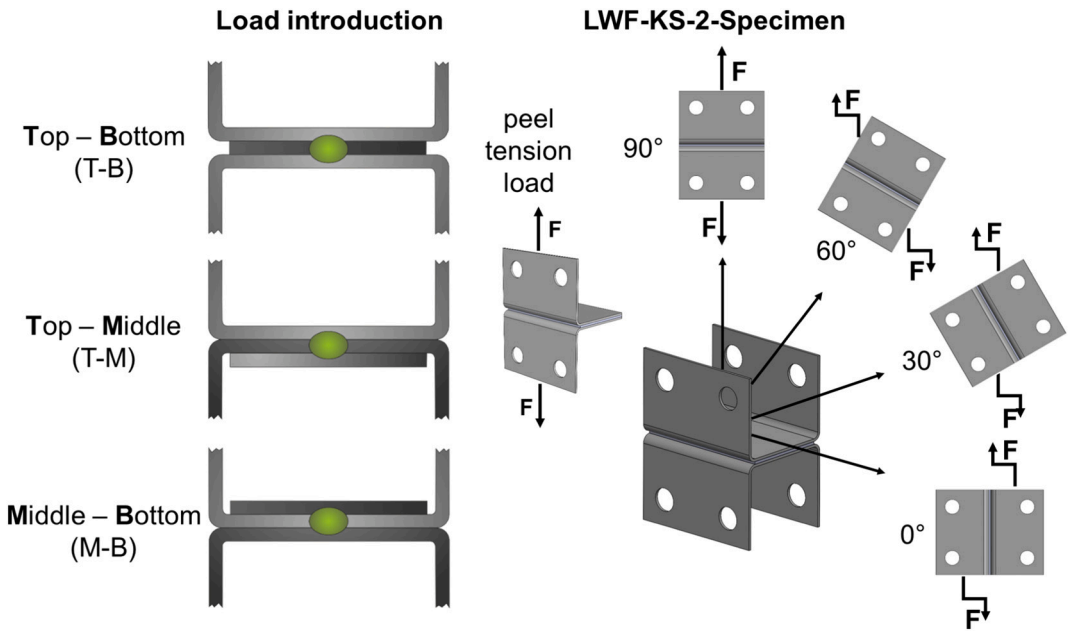

Fig. 1. Schematic representation of the three load introductions and the different loading orientations of the LWF-KS-2 specimen.

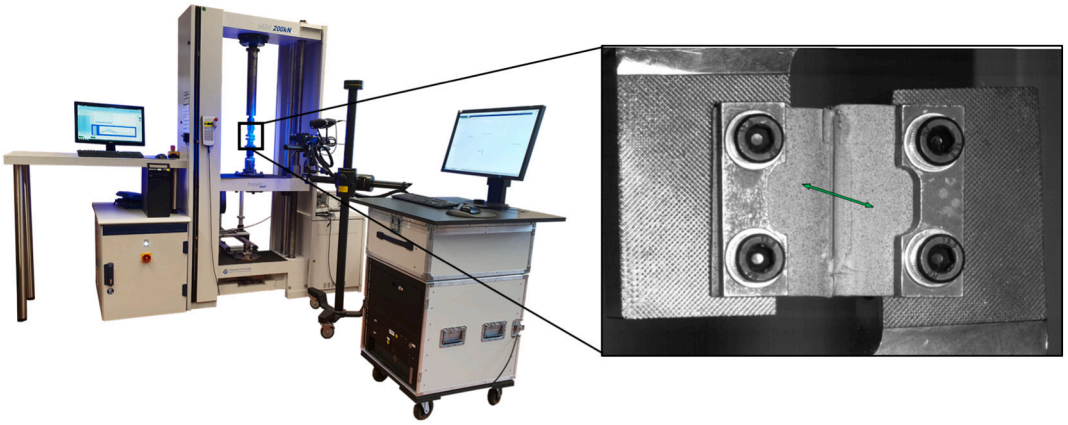

Fig. 2. LWF-KS-2 specimen in the testing machine for shear testing, with an arrow indicating the position of the measuring points.

ensures that the observed fracture mechanisms in the LWF-KS-2 tests can be directly linked to the underlying microstructural and mechanical property distributions within the FZ, HAZ, and BM.

The fractured weld nuggets were examined by measuring the fracture surface with a microscope and examining micrographic cross-sections of the tested samples. The failure modes of RSW joints can be classified into different types of fractures according to [24,39,46]: interfacial fracture, button pull-out fracture, dome failure, and tear-out fracture. According to the literature, spot welds experience two forces during loading: the tensile force in the normal direction to the weld interface and the shear force in the vertical direction to the weld interface [18]. In the case of button pull-out failure, the fracture surface revealed that the tensile force was dominant, and the failure involved localized plastic deformation through the sheet thickness.

2.4. Finite element method simulation

The numerical investigation of the load-bearing capacity was conducted using the finite element software LS-DYNA Version R11.1.0. The models were constructed based on real specimen geometries and calibrated against experimental results. Material behavior was modeled using the LS-DYNA material cards MAT_24 and MAT_ADD_DAMAGE_GISMO.

Fig. 3 shows the boundary conditions for a representative three-layer model under shear loading (joint F). The implemented model includes HAZ for CR300LA and HCT590X. No data or experimental results were available for an exact calibration of the weld nugget material of the dissimilar welds. Therefore, in the case of joint F, the interfacial zone of the weld nugget was modeled with the HC340LA HAZ material, while the rest of the weld nugget was modeled with HCT590X weld nugget material. This combination led to the results with the best agreement to the experimental results. All material cards were calibrated using either literature data or material testing, while a custom model for CR1900T was developed specifically for this study [47].

To ensure accurate representation of the failure behavior, the geometry of the weld nugget was extracted from three metallographic cross-sections and averaged. A Bézier curve was used to recreate the FZ contour within the mesh, improving the representation and mesh quality in the critical region. The simulation mesh used an element edge length of 0.1 mm and ELFORM 1. To reduce computation time, the upper specimen half (NMOV) was moved at 0.5 m/s along the y-direction, while rotations around the x-axis were allowed. The lower half (NFIX)

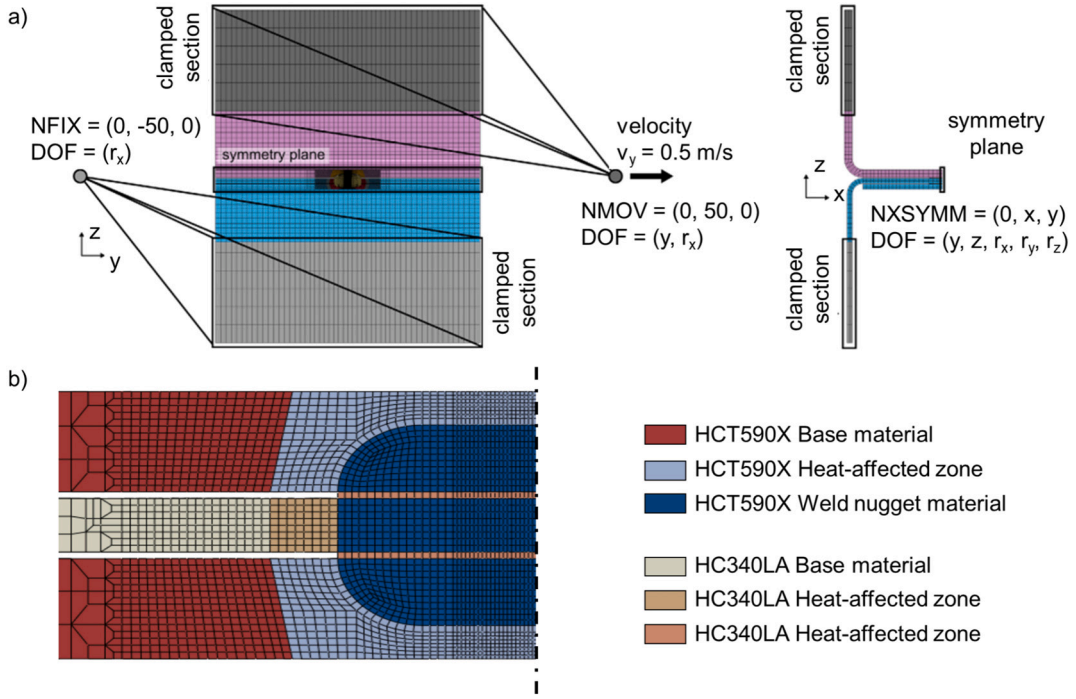

Fig. 3. a) Boundary conditions for the finite-element model for shear loading, and b) mesh at the weld nugget and material.

was fixed in all directions except for rotation around the x-axis [47].

These boundary conditions were defined to replicate the geometry and constraints of the experimental LWF-KS-2 fixture. In particular, the fixation of the lower specimen half and the allowed rotations of the upper half directly mirror the clamping and loading conditions applied in the physical setup, thereby ensuring consistency between the numerical and experimental configurations.

In preliminary simulations, electrode indentation was explicitly modeled. However, its influence on the global load-displacement behavior and predicted load-bearing capacity was found to be negligible. To reduce modeling complexity and computational cost, electrode indentation was therefore omitted in subsequent simulations. This simplification is consistent with previous studies, which demonstrated that neglecting electrode indentation under controlled conditions yields nearly identical load-bearing predictions [48].

2.5. Methodology for model development and optimization

To develop a reliable prediction model for the load-bearing capacity of two- and three-layered joints, a combination of physical modeling, statistical analysis, and algorithmic optimization was employed. The core objective was to derive robust yet practical equations capable of estimating peak loads based on accessible input parameters such as nugget diameter, sheet thickness, and ultimate tensile strength of the base material.

The analysis was based on an extended dataset including newly conducted experiments and reference data from literature [19]. First, a correlation and regression analysis were carried out separately for shear- and tensile-dominated failure. Relevant input variables were identified using Pearson and Spearman coefficients, and their influence was quantified through linear and second-order polynomial regressions. To address multicollinearity, the variance inflation factor (VIF) was calculated, and variables with VIF > 5 were excluded to ensure numerical stability. Each governing failure mechanism, interfacial fracture, button pull-out, and tear-out, was described by a physically interpretable model. These were formulated using characteristic geometric and material parameters, such as nugget area or perimeter, and adjusted using statistically derived calibration functions.

To fine-tune the model coefficients, an optimization based on the evolution strategy was applied (Fig. 4). This method, part of the class of evolutionary algorithms, follows the principle of biological evolution: candidate solutions are represented as parameter vectors and iteratively improved through recombination, mutation, and deterministic selection of the fittest individuals [49]. In this study, a $(\mu + \lambda)$ strategy was used with a parent population size of $\mu = 30$ and $\lambda = 100$ offspring per generation. The optimization was repeated for $\lambda = 100$ generations per failure mode using the CVA Python package developed by Divis Intelligent Solutions [50]. The crossover rate was set to 0.7, while the mutation rate was set to 0.2, following established practice for evolutionary algorithms. To ensure physical plausibility, artificial data points were introduced to enforce logical boundary conditions, e.g., zero load at zero strength or thickness. Additionally, constraints on gradient behavior were used to capture the experimentally observed saturation of load-bearing capacity at high-strength levels.

This methodical approach allowed the creation of validated models that combine physical interpretability with high predictive accuracy. The final prediction formulas were optimized and tested against independent experimental data not used for training.

3. Results and discussion

3.1. Validation of the welding parameters

The welding parameters listed in Table 3 were validated experimentally for all nineteen joining configurations. The validation aimed to ensure a consistent and nearly symmetrical nugget geometry with a target nugget diameter of approximately $5\sqrt{t_{min}}$ at each interface, thereby enabling comparability across all test configurations. In addition to geometric verification, microhardness measurements were carried out to assess the potential influence of the weld zone properties on failure behavior. All metallographic and hardness results are documented in Table 4.

A representative cross-section and the corresponding hardness distribution of the 3-LJ, configuration C, are shown in Fig. 5. The FZ consists of two different martensitic microstructures: a columnar martensitic structure in the outer layer, resulting from rapid

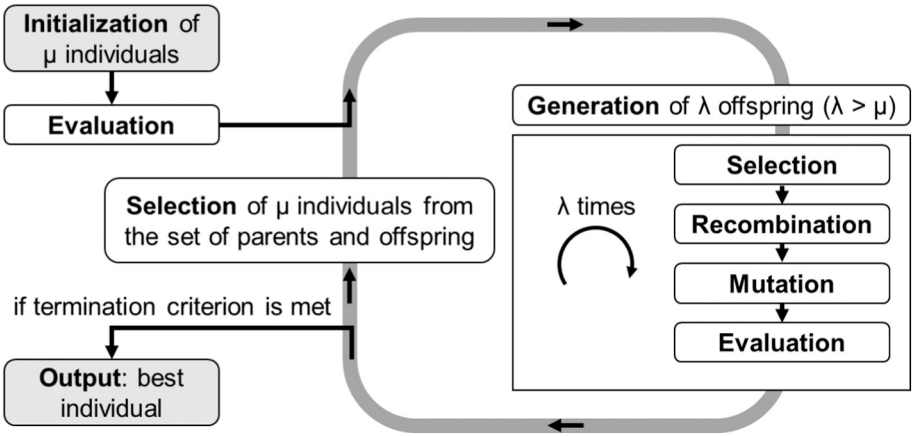

Fig. 4. Process of an evolutionary algorithm based on [49].

Table 4
Cross-section-based sampling parameters (average of three specimens).

No.	FZ diameter T-M in mm	FZ diameter M-B in mm	HAZ diameter in mm	FZ hardness in $HV_{0.1}$	Softened HAZ hardness in $HV_{0.1}$	HAZ hardness in $HV_{0.1}$
a	4.88	–	5.98	–	–	–
b	4.80	–	6.51	–	–	–
c	4.07	–	6.95	–	–	–
d	5.33	–	7.12	–	–	–
e	5.10	–	6.86	–	–	–
f	4.77	–	6.64	573	386	697
g	4.95	–	7.05	–	–	–
h	5.10	–	6.60	624	409	685
i	5.04	–	6.76	539	393	688
j	5.07	–	6.14	–	–	–
k	4.90	–	6.40	–	–	–
l	5.54	–	7.81	–	–	–
A	4.48	4.69	7.93	543	397	680
B	4.76	4.92	7.63	500	388	654
C	5.00	4.22	7.21	454	391	695
D	5.22	4.49	7.38	452	405	680
E	4.70	4.72	7.50	557	394	688
F	6.49	6.72	8.83	367	390	204
G	5.39	4.83	8.22	452	405	680

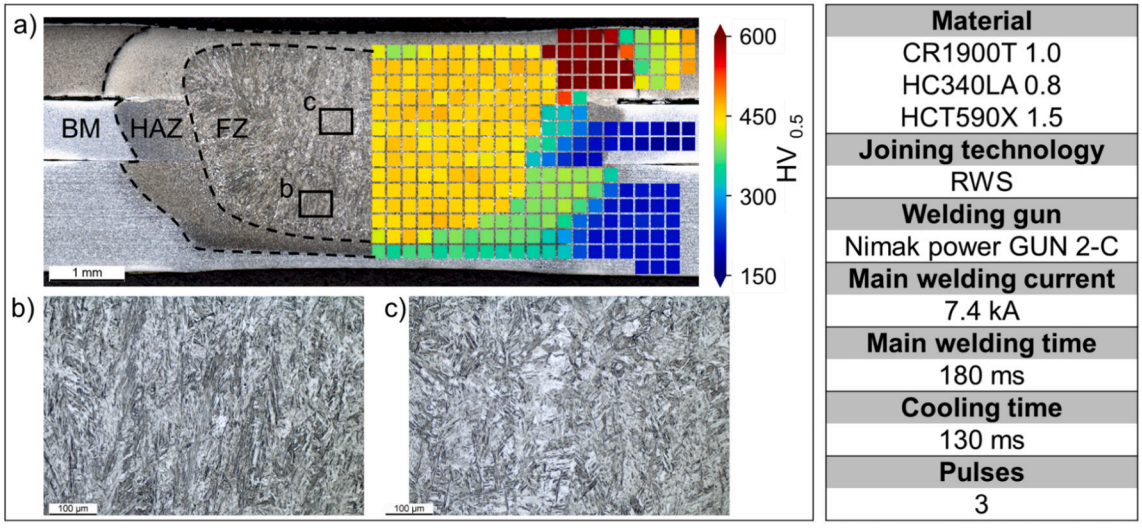

Fig. 5. a) Cross-section and hardness characteristics of the three-layered joint C, with FZ, HAZ, and BM indicated; b) and c) Comparison of microstructure of the FZ.

solidification, and an equiaxed structure of prior austenite grains in the inner core.

The hardness mapping results reveal pronounced differences among the BM, the HAZ, and the FZ. The FZ, which undergoes complete melting and resolidification during welding, exhibits a hardness of 545 ± 10 HV. The HAZ, although not molten, undergoes significant microstructural

transformation, while the BM remains unchanged. The hardness values in the HAZ and BM of HCT590X and HC340LA are substantially lower than those in the weld nugget. In contrast, the HAZ of CR1900T displays significantly higher hardness. The employed welding schedule, which was optimized to suppress halo formation, proved to be effective. No softening at the fusion boundary (halo) was observed.

3.2. Experimental characterization of joint failure behavior

To understand the transferability of the mechanical behavior from 2-LJ to 3-LJ, it is essential to assess the load-bearing capacity of 2-LJs. For this purpose, twelve 2-LJ specimens were tested, including symmetric joints with identical materials and dissimilar material combinations. The objective was to identify correlations. In addition to force–displacement curves, fracture locations and modes were examined.

3.2.1. Two-layer joints

Fig. 6 compares the experimentally determined peak loads across different loading angles for both similar and dissimilar 2-LJ. For all material combinations, the load-bearing capacity decreased with increasing load angle. The highest peak loads were observed under shear-dominated loading (0°) and the lowest under peel loading. At 60° and 90°, a plateau in peak load was observed.

Among the similar joints (a - e), the results show that under shear-dominated loading (0°), the peak load correlates with the base material strength, up to an upper threshold. For instance, joints made of HCT590X or CR1900T reached high peak loads of approximately 14.0–14.6 kN, whereas joints made of HC340LA achieved lower values around 7.1 kN. But this effect diminishes for ultra-high-strength steels. For example, while the ultimate tensile strength of CR1900T exceeds that of HCT780X, no further increase in shear peak load is observed. The dominant factor becomes the fracture mode rather than the material strength.

Under tensile-dominated conditions (90°), high-strength steels such as CR1900T showed pronounced sensitivity to tensile stress and failed at low forces (≈2.1 kN) due to brittle button pull-out or mixed-mode fractures with limited plastic deformation. Cracks typically initiate along the fusion boundary, where a steep hardness gradient toward the softened HAZ exists. In contrast, ductile steels maintained moderate performance and exhibited more plastic deformation prior to failure.

In contrast, dissimilar joints exhibited a wider range of failure behaviors depending on the material combination. In general, the fracture locations could be reliably predicted using the minimum principle, whereby failure occurs in the weaker sheet material when tested as a symmetric 2-LJ. To enable a quantitative assessment of joint strength, the concept of equivalent similar joint strength (ESJS) was introduced. The ESJS defines the characteristic load-bearing capacity of a spot weld between two identical sheets of a given material under a defined load orientation. It provides a material-specific benchmark for predicting failure locations in dissimilar joints, based on which sheet has the lower ESJS. This enables the application of the minimum principle across different material combinations and load cases.

Nonetheless, deviations were observed depending on joint stiffness. Stiffer joints suppressed nugget rotation and thereby reduced the effective normal stress, improving load-bearing capacity under shear. For instance, the CR1900T-HCT590X joint (g) achieved higher shear strength than either of its similar references (c and e), due to improved geometric stiffness and less rotation. Conversely, joints with more ductile materials facilitated greater rotation under load, increasing the effective tensile stress and leading to early failure, even below the strength of the weaker reference.

These findings are further corroborated by the observed fracture modes. Under shear loading, low-strength steels such as HC340LA tended to fail via button pull-out failure with high deformation, whereas ultra-high-strength materials like CR1900T failed with minimal plastic deformation. Fig. 7 illustrates the range of fracture modes, with similar joints typically failing through double-sided button pull-out failure and dissimilar joints more often showing single-sided button pull-out failures. Special cases, such as mixed-mode fractures with partial tear-out, were observed in joints involving CR1900T, particularly under peel

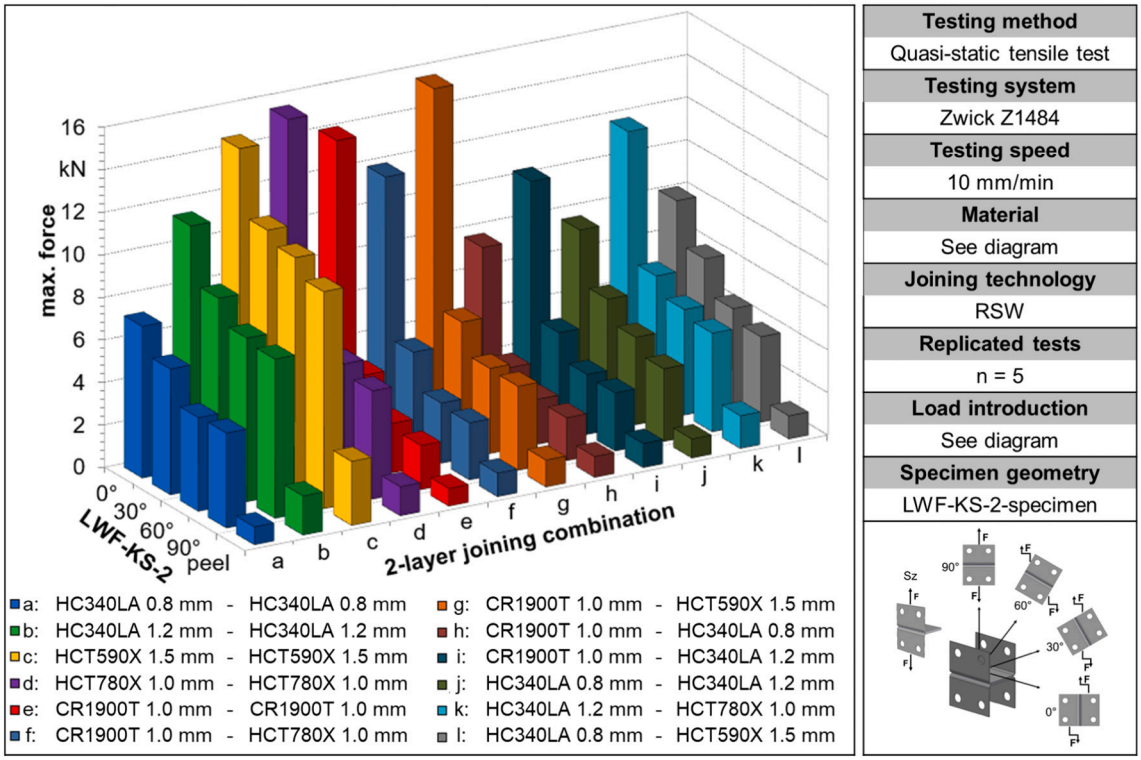

Fig. 6. Maximum forces for two-layer joining configurations.

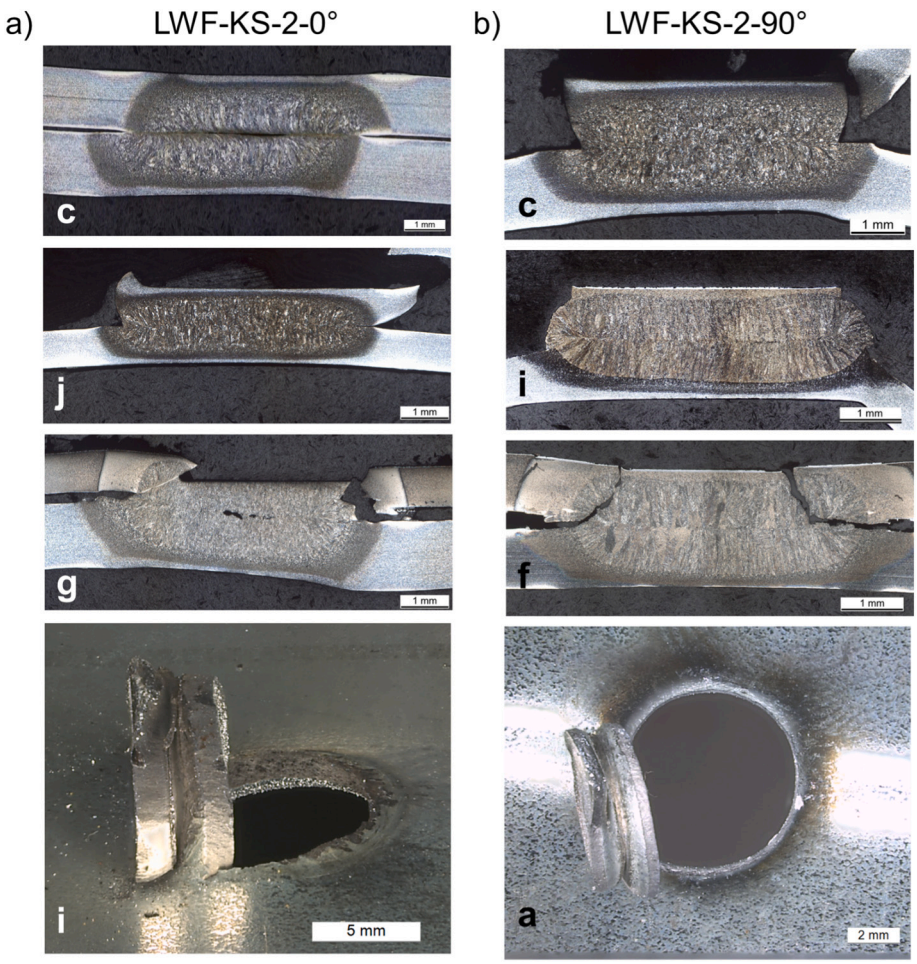

Fig. 7. Failure behavior of representative 2-LJ under shear and cross-tension loading.

and tensile-dominated loading.

In summary, the analysis of two-layer joints confirms that the load-bearing capacity can be effectively described by the minimum principle, with failure typically governed by the weaker joining partner. In addition, joint stiffness and the resulting degree of nugget rotation were identified as critical factors influencing effective stress distribution and failure mode transitions. These findings provide an essential foundation for the subsequent analysis of three-layer joints. In particular, the principles established for 2-LJ, minimum principle, stiffness effects, and fracture mode dependence on material strength serve as a reference framework to assess whether and how they can be transferred or adapted to the more complex behavior of 3-LJ.

3.2.2. Three-layered joints

The load-bearing capacity of 3-LJ is significantly influenced by the method of load introduction. Unlike 2-LJ, 3-LJs allow for multiple loading configurations due to the presence of an additional layer. In this study, the load was introduced into two of the three sheets, resulting in three distinct configurations: top–bottom (T–B), top–middle (T–M), and middle–bottom (M–B). The third, non-loaded sheet is referred to as the passive sheet. Each configuration was tested under various loading angles to systematically assess the effects of stacking sequence, material properties, and passive sheet behavior on the joint's mechanical response.

In the case of T–B loading, the load-bearing capacity is largely dictated by the weaker of the two outer sheets, while the middle sheet mainly stabilizes the configuration without directly initiating fracture. For T–B loading, where the outer sheets are actively loaded and the middle sheet serves as the passive layer, the results showed that the load-bearing capacity was governed by the weaker of the two outer sheets. This observation aligns with an extended interpretation of the minimum principle for 3-LJ, whereby failure occurs in the outer sheet with the lower ESJS. However, subtle differences in failure behavior were observed depending on the properties of the passive sheet.

Fig. 8 compares two joints, C and E, with identical outer sheets (CR1900T and HCT590X), but different middle sheets (HC340LA vs. CR1900T). Although the middle sheet is not directly loaded, it had a significant impact on the hardness distribution within the weld nugget and consequently influenced the failure mode. Both joints failed via a combination of button pull-out and dome failure under tensile-dominated loading. However, the harder FZ in joint E led to a more brittle fracture response, whereas the softer nugget in joint C promoted greater ductility. These highlight the indirect yet critical role of the passive middle sheet in governing fracture mechanisms and energy absorption behavior.

Overall, these results confirm the minimum principle for T–B loading, since failure consistently followed the weaker outer sheet. This behavior establishes a clear baseline for the subsequent analysis of three-layer joints.

Under T–M loading, fracture behavior is usually governed by the outer sheet subjected to direct load, though premature tearing of the middle sheet may arise when its thickness or strength is comparatively low. When the load was introduced into the top and middle sheet (T-M), the joints generally failed in the outer (top) sheet. However, deviations from this trend were observed when the middle sheet possessed significantly lower mechanical strength or reduced thickness. In Joint F and C

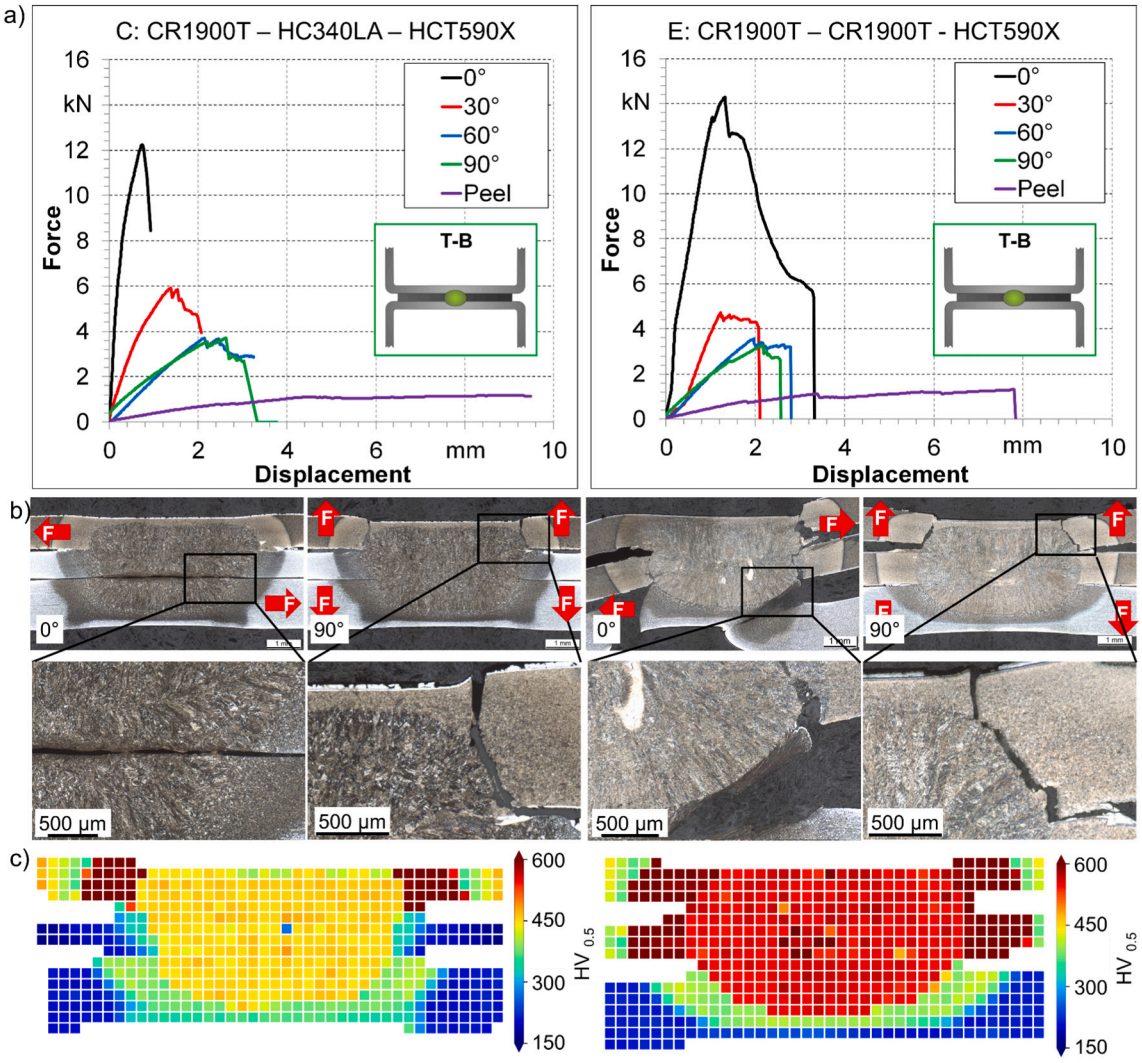

Fig. 8. a) Force-displacement curves, b) fracture surfaces, and c) hardness mapping for the T-B load introduction case.

(Fig. 9), both using a 0.8 mm thick HC340LA as the middle layer, failure was initiated by tear-out fracture within the middle sheet. This behavior was particularly pronounced under shear-dominated loading. The limited load-carrying capacity of the thin HC340LA sheet was insufficient to sustain the applied forces, resulting in premature failure through base material tearing.

Further analysis revealed a secondary failure mode in the passive sheet of joint C. Due to deformation of the middle HC340LA layer, a bulge formed at the weld interface (Fig. 10), introducing a tensile stress component in the passive outer CR1900T sheet. This stress led to crack initiation at the nugget boundary, causing button pull-out from the passive sheet. Secondary cracking of this type was only observed in joint C under T–M loading, corresponding to approximately 5 % of all specimens tested under 0° loading. However, as evidenced by the load-displacement curve, this secondary failure had no significant effect on the overall load-bearing capacity of the joint.

Taken together, the T–M results emphasize the decisive role of the middle sheet: depending on its relative thickness and strength, it may either remain passive or initiate fracture, marking an important transition for 3-LJ predictions.

For M–B loading, the joint strength is typically governed by the bottom sheet, but pronounced plastic deformation of the middle sheet can redistribute stresses and trigger complex fracture sequences involving the passive outer sheet. In the M–B configuration, where the load is introduced through the middle and bottom sheets, failure typically initiates in the actively loaded outer (bottom) sheet. However, when CR1900T served as the passive sheet, as in joint C, additional failure mechanisms were identified. The key factor here is the mechanical behavior of the middle sheet, a thin HC340LA (0.8 mm) with relatively low tensile strength and high ductility. Under loading, this sheet undergoes substantial plastic deformation, which induces an upward force on the passive CR1900T sheet and results in tensile stress (Fig. 11(c)). According to existing research [51], increased softening in the HAZ of PHS RSW joints reduces their tensile load-bearing capacity and results in failure in the SHAZ. The tensile load-bearing capacity is also reduced by the brittle microstructure along the boundary between the CR1900T HAZ and the weld nugget. This explains why joints containing press-hardened steels with higher nominal UTS values do not necessarily achieve higher load-bearing capacities. The combination of local HAZ softening and the inherently brittle martensitic microstructure promotes premature crack initiation and unstable propagation along the nugget boundary, effectively reducing joint strength despite the higher base material strength. The upward force on the passive CR1900T results in the formation of radial cracks. These cracks propagate, leading to button pull-out failure in the passive sheet.

As illustrated in Fig. 11, this initial failure does not immediately terminate load transmission. Instead, a second load path becomes active, transferring the remaining force through the bottom and middle sheets. The force increases again until the weld nugget is pulled out of the deformed middle sheet (HC340LA), completing the two-stage failure

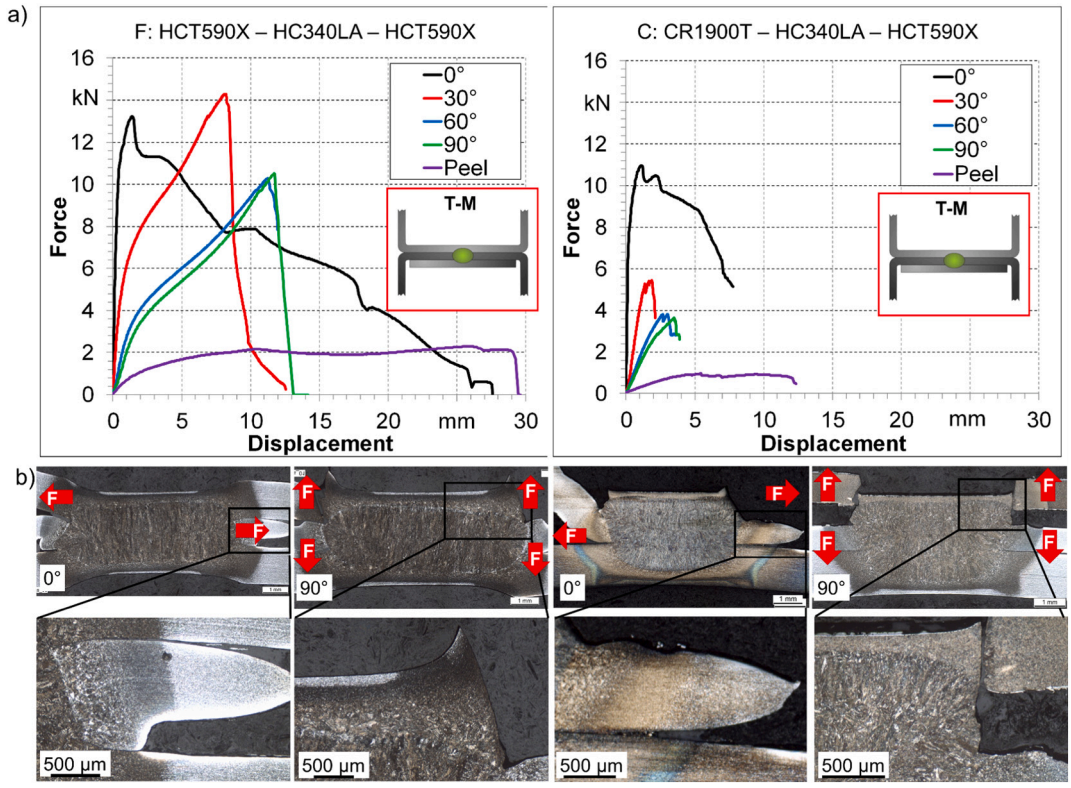

Fig. 9. a) Force-displacement curves, b) fracture patterns, and sections of the tested specimens for the T-M load introduction case.

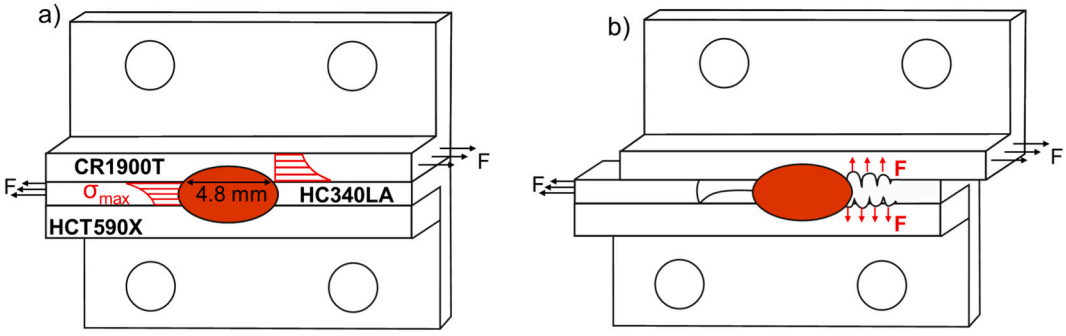

Fig. 10. Schematic bulge formation and secondary fracture mechanisms.

process. Two-stage failure of this type was only observed in joint configuration C under M–B loading, occurring at 60°, 90°, and peel orientations. The frequency was approximately 5 % of the specimens tested under each of these orientations. The sequential activation of multiple fracture paths resulted in a distinct stepwise force-displacement response, with the outer and middle sheets failing successively. This behavior highlights the significant influence of stress redistribution in three-layer joints and its impact on the fracture process.

This behavior differs significantly from joint G, where the passive outer sheet is CR1500T, a press-hardened steel (PHS). The effect of lowered load-bearing capacity under tensile loading is not as pronounced for the SHAZ and HAZ of the CR1500T sheet compared to the CR1900T sheet. While microcracks were observed in the CR1500T sheet under similar loading conditions, complete button pull-out was avoided due to its higher tensile loading resistance. Instead, the maximum load was reached when the tensile load-bearing capacity of the outer, actively loaded sheet (HCT590X) was exceeded, leading to a single-stage failure through button pull-out fracture in this layer.

This comparison highlights how the mechanical properties of the passive outer sheet, specifically its microstructural changes in the HAZ caused by the welding process, critically influence the occurrence of secondary failure mechanisms. The experimental results further confirm that the load-bearing capacity under tensile loading for spot-welded joints containing press-hardened steels (PHS) is inversely related to the ultimate tensile strength of the base material, as previously observed in [51]. A higher ultimate tensile strength of the base material of PHS leads to a lower load-bearing capacity of the spot-welded joint under tensile loading.

In conclusion, the M–B results underline the strong influence of middle sheet stiffness on load redistribution and fracture progression. This mechanism introduces additional complexity into 3-LJ joints and must be accounted for in predictive models.

3.3. *Numerical investigation of failure mechanisms in three-layered joints*

To complement the experimental observations and gain deeper insight into the complex failure mechanisms of 3-LJ, finite element simulations were performed using selected configurations. The

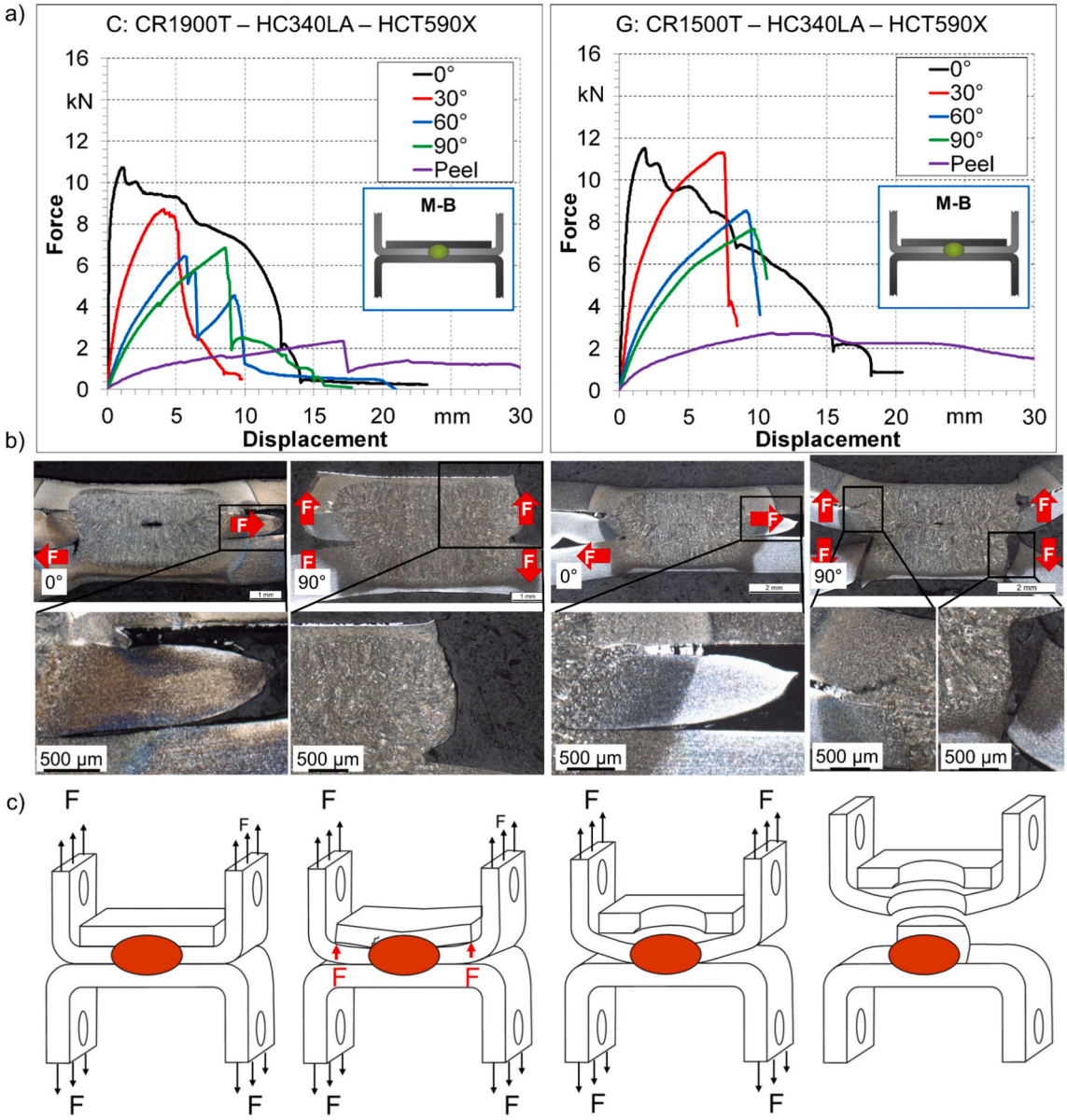

Fig. 11. a) Force-displacement curves, b) fracture patterns and sections of the tested specimens, and c) schematic fracture path for the M-B load introduction case.

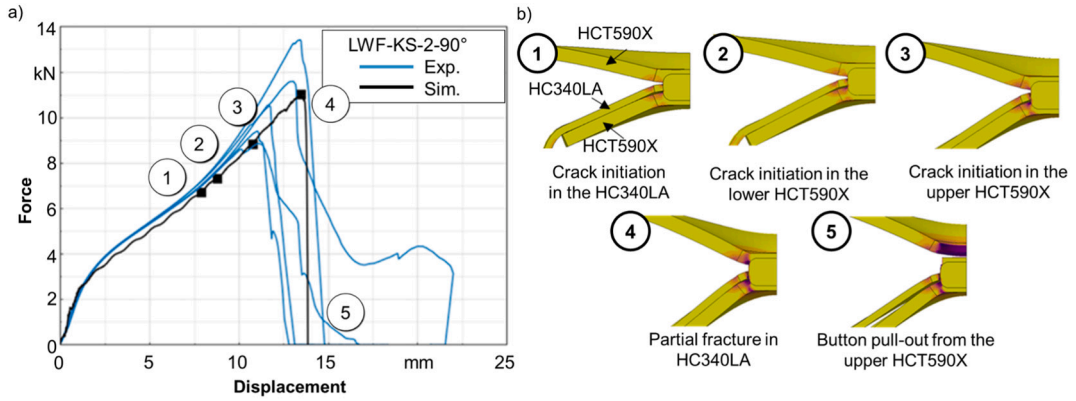

Fig. 12. a) Comparison of simulated and experimental force-displacement curves and b) deformation for joint F (M–U).

simulations aimed to evaluate the influence of geometric and material parameters, particularly the thickness of the middle sheet, on deformation behavior and spot weld rotation. In addition, variations in nugget geometry were introduced to assess their impact on load-bearing capacity and failure modes.

3.3.1. *Influence of the middle sheet thickness and weld nugget diameter*

To isolate the influence of the middle sheet, a parametric study was carried out based on joint F. To ensure the reliability of the parametric study, the baseline configuration (joint F) was validated against experimental results. Fig. 12 compares the calculated and measured force-displacement curves and shows the corresponding simulated deformation at selected points. Both maximum force and displacement at fracture lie within the experimental scatter, confirming the predictive capability of the FE model. The deformation fields reproduce the characteristic sequence of crack initiation in the HAZ, subsequent tearing, and final button pull-out, in good agreement with the observed failure process. The supporting effect of the passive sheet, which constrains the bending of the middle sheet, is also well captured. Without this effect, premature failure of the middle sheet would have occurred. These results demonstrate that the developed FE model can reliably represent the load-bearing behavior under quasi-static loading.

Variants with different middle sheet thicknesses (0.8 mm and 1.5 mm) and materials (HC340LA and HCT590X) were simulated. The results, shown in Fig. 13, reveal that increasing the thickness of the middle sheet at T-M loading significantly enhances joint stiffness and reduces deformation. This reduction in deformation is primarily caused by the suppression of nugget rotation, as a thicker middle sheet constrains relative movement between the outer layers and lowers the tensile stress component acting normal to the weld. As a secondary effect, the thicker middle sheet also promotes a more even redistribution of stresses across the joint, further stabilizing the load-bearing behavior.

However, the effect of the middle sheet's material was found to be less pronounced. Regardless of the alloy used, the deformation of the outer loaded sheet remained largely unaffected, indicating that load-bearing capacity in this load case is primarily governed by the outer layer.

In contrast, for T–B loading (passive middle sheet), simulations confirmed that neither the thickness nor the material of the middle sheet had a noticeable effect on the global deformation pattern or maximum load at tensile loading. These findings support the experimental results, highlighting that the middle sheet does not contribute to the joint's tensile load-bearing capacity when not actively engaged in load transfer.

Beyond material and geometric properties, the influence of nugget size was also investigated. Using configuration F under T–M loading, two nugget diameters were simulated. A smaller nugget led to plastic deformation along the whole diameter in the base material of the middle sheet around the spot weld, promoting early failure through bulging and tear-out fracture. As shown in Fig. 14, this deformation behavior is consistent with the experimentally observed “bulging” in the middle sheet. In contrast, a larger nugget distributes the applied load over a wider area, thereby reducing stress concentration and delaying the initiation of failure. The element deletion shown in the simulations was governed by the LS-DYNA material model MAT_ADD_DAMAGE_GISSMO, using the failure criterion $D \geq 1$, where D denotes the accumulated path-dependent damage. Each damage increment ΔD was calculated as $\Delta\varepsilon/\varepsilon_f$, with ε_f being the fracture strain as a function of stress triaxiality and Lode angle. For ε_f, a Hosford-Coulomb model was applied. The elastic-plastic parameters and Hosford-Coulomb constants for the base material, HAZ, and FZ were calibrated according to [52].

3.3.2. *Influence of the weld nugget rotation*

Additional simulations were performed for joint B to study the influence of the joint stiffness on the failure mode. The rotation of the weld nugget varies during loading and varies depending on the load introduction. The following simulations serve to highlight the correlation between load path and rotational behavior of the spot weld (Fig. 15). Under T–B loading, the weld experienced significantly more rotation compared to M–B configurations. This increased rotation elevates the tensile stress component on the spot weld, thereby reducing the load-bearing capacity. In contrast, M–B loading suppressed weld rotation due to higher rotational constraint from the thicker bottom sheet, resulting in higher peak loads.

The observed differences in rotational behavior can be attributed to the variation in joint stiffness associated with different load introduction paths. In T–B loading, stiffness is lowest because the load is applied to two outer sheets. The increased distance between the load application points allows the weld to rotate more freely. Conversely, in M–B loading, the load is introduced through the middle and one outer sheet, while the second outer sheet serves as a passive support. This configuration

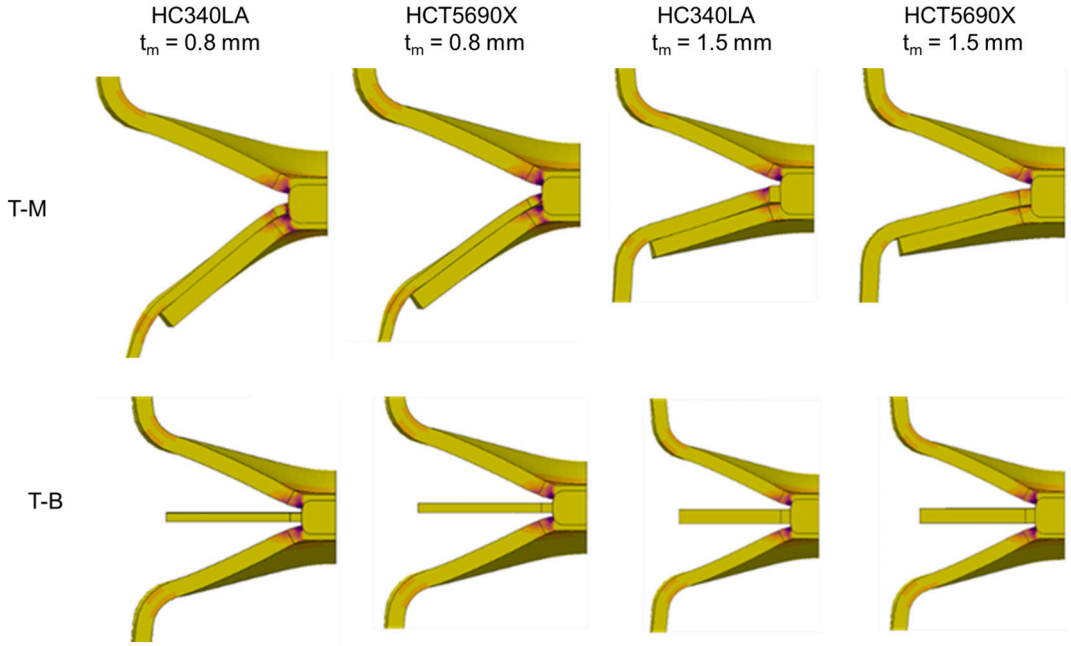

Fig. 13. Simulated deformation behavior for configuration F under T–M and T–B loading with varying middle sheet thickness (t_m) and material.

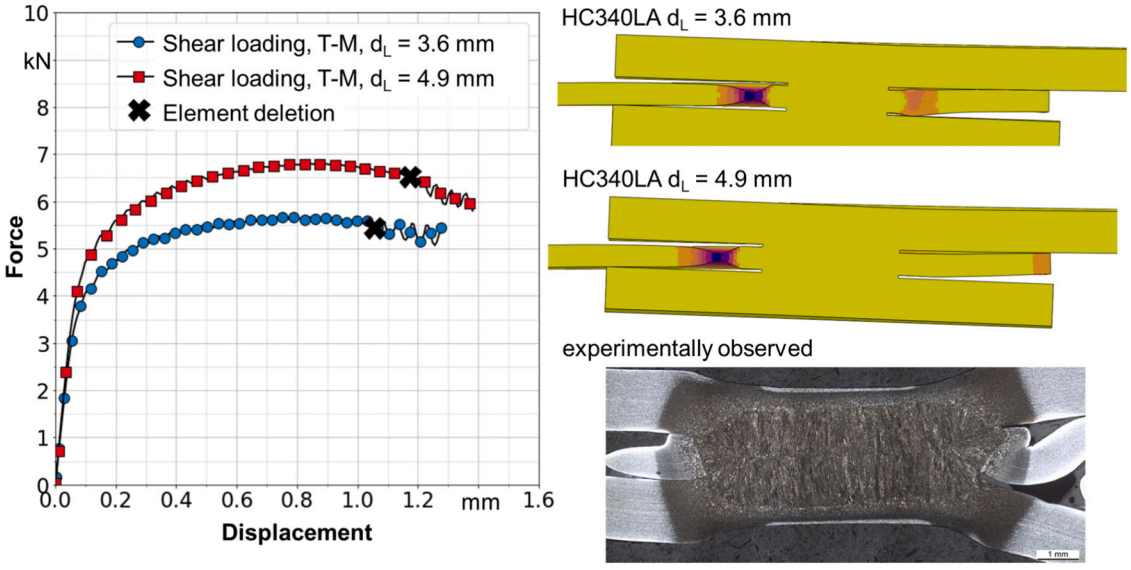

Fig. 14. Influence of nugget size on plastic strain and force-displacement response.

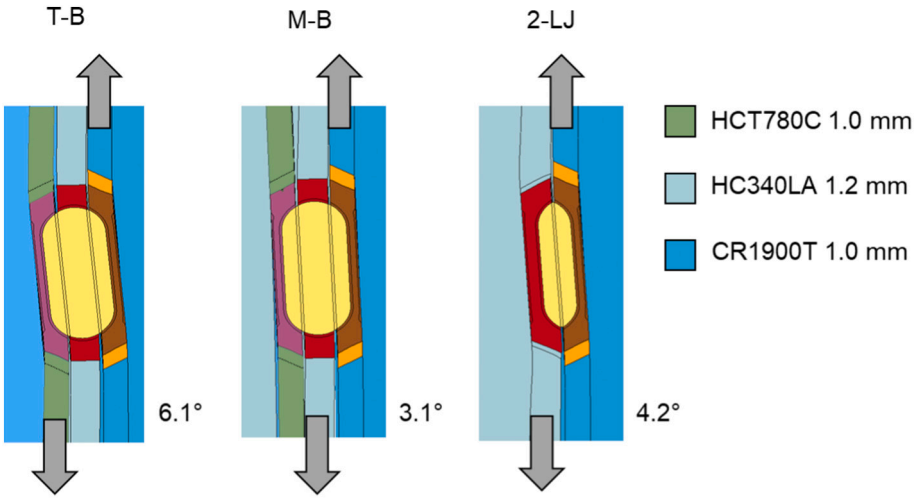

Fig. 15. Comparison of weld rotation under T–B, M–B, and 2-LJ loading conditions.

enhances the structural constraint around the nugget, increasing the effective stiffness of the joint and thereby limiting rotational degrees of freedom.

These numerical findings confirm that nugget geometry and joint stiffness can serve as indicators in determining the failure mode and effective load distribution. Specifically, nugget size and middle sheet stiffness govern the stress path and rotational freedom at the weld, both of which impact the joint's load-bearing capacity.

3.4. Method for transferring load-bearing predictions from 2-LJ to 3-LJ

To enable the predictive modeling of 3-LJ, it is essential to assess the extent to which the established relationships identified for 2-LJ can be transferred to 3-LJ. While many mechanical principles remain valid, the addition of a third sheet introduces new interactions, especially regarding load paths, joint stiffness, and nugget asymmetry, that must be systematically considered.

Across both 2-LJ and 3-LJ, the load orientation (θ) was found to be a primary influencing factor. With increasing normal load component (from 0° to 90°), the maximum transferable load consistently decreased. However, an increase in joint stiffness is primarily observed in 3-LJ when the load is introduced through the middle and one outer sheet. In such configurations, weld rotation is more constrained, reducing the effective normal stress in the weld zone under shear-dominated loading and thereby increasing the load-bearing capacity. In contrast, when the load is applied through both outer sheets (T-B), weld rotation may even exceed that of 2-LJ. Under tensile-dominated loading, the altered stiffness distribution shifts the location of stress concentration close to the joint root.

The nugget diameter directly defines the effective load transfer area and shows a linear correlation with peak load across all configurations. However, in 3-LJ, each interface forms its own nugget diameter. Therefore, the relevant nugget diameter must be considered depending on the specific load introduction path, as load transfer occurs primarily across the interface between the actively loaded sheets.

Material strength continues to play a key role in defining the joint capacity. For 2-LJ, load-bearing capacity initially increases with tensile strength before stagnating or decreasing due to brittle fracture modes. This principle also applies to 3-LJ: the load-bearing capacity is governed by the strength of the loaded outer sheet, unless the middle sheet becomes the limiting factor due to localized deformation.

Importantly, the stacking sequence of materials significantly affects

load-bearing capacity in 3-LJ. Placing the weaker material in the middle allows it to be supported by the outer sheets, thereby preventing early button pull-out and increasing joint capacity. Conversely, if the weaker sheet is located on the outside and actively loaded, it will limit the joint strength. This observation aligns with the extended application of the minimum principle for 3-LJ: when the outer sheet fails, the joint capacity is determined by its ESJS. However, if the material in the middle exhibits a lower **tensile strength-to-thickness ratio** compared to the outer sheet, a secondary fracture mode such as middle sheet tear-out (e.g., joint F, T-M, joint C, M-B, and joint G, M-B) or even failure of the passive outer sheet may occur (e.g., joint C, T-M).

Based on these findings, a decision tree was developed to support the transfer of predictive principles from 2-LJ to 3-LJ. The decision tree shown in Fig. 16 provides a rule-based framework for predicting the dominant failure mode in 3-LJ.

The branching criteria are based first on the load introduction path (T–B, T–M, or M–B), followed by the relative tensile strength-to-thickness ratios of the interacting sheets. In this context, "strong deformation of the middle sheet" is defined as a condition where the normalized thickness-to-strength ratio of the middle sheet is significantly lower than that of the outer sheets. Under such conditions, the middle sheet undergoes pronounced plastic deformation, which may trigger secondary fracture mechanisms such as middle-sheet tear-out or even failure of the passive outer sheet.

When the middle sheet is weaker than the actively loaded outer sheet, the tree predicts middle-sheet tear-out. Conversely, when the outer sheet is weaker, button pull-out dominates. Additional branches account for interfacial fracture when nugget size or strength ratios fall below critical thresholds. The tree was constructed using the experimental database. It correctly predicted the dominant failure mode in approximately 95 % of all tested configurations. This predictive accuracy demonstrates that the decision tree provides a robust foundation for

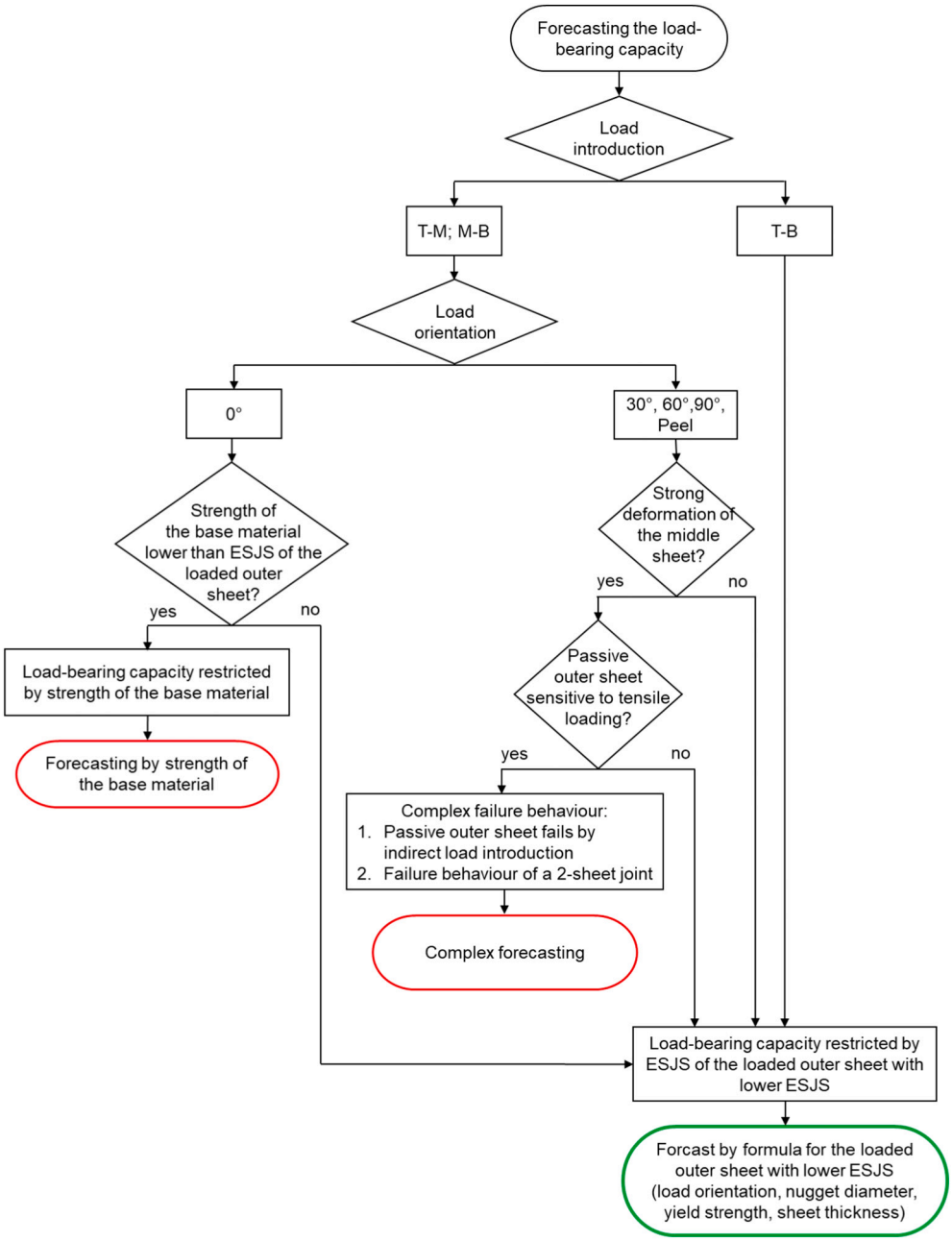

Fig. 16. Flow chart for determining the applicable prediction method and dominant failure path in three-layer spot welds.

the subsequent development of analytical prediction formulas.

In summary, the transferability of principles from 2-LJ to 3-LJ can be grouped into three categories. First, principles such as the minimum principle and the linear correlation between nugget diameter and load capacity can be directly transferred. Second, stiffness-related mechanisms require modification, since the middle sheet alters nugget rotation and stress redistribution compared to 2-LJ. Third, stacking-sequence effects and secondary fracture modes are unique to 3-LJ and must be explicitly accounted for in predictive models. This structured classification provides a coherent framework for linking experimental observations with the subsequent model development in Section 3.4.

3.5. Prediction model development

Based on the findings in Sections 3.1 to 3.3, an analytical prediction method was developed to estimate the maximum force of 2-LJ and 3-LJ configurations. The development process began with a statistical analysis of experimental data to identify the most relevant input variables. By evaluating correlations and regression performance, four key parameters were selected for model formulation: nugget diameter, sheet thickness, ultimate tensile strength of the failing sheet, and the normalized tensile strength-to-thickness difference between sheets. Variables with low explanatory power or high multicollinearity were systematically excluded to ensure robustness and transferability.

The core of the model consists of physically derived formulations for each observed failure mode: interfacial fracture, button pull-out, and tear-out. Each mode was described by a tailored function calibrated with experimental data. The transition between failure modes was captured using an extended minimum principle, which ensures that the predicted strength corresponds to the weakest actively loaded element in the joint. Model calibration and validation were performed using experimental data from this study and [19], supported by an evolutionary optimization strategy [49,50].

Under shear loading, the model achieved excellent accuracy. The load-carrying capacity in shear fracture was described as a function of the nugget diameter d_L and the shear tensile strength of the FZ τ_{SG}, corrected by a stiffness-dependent scaling factor α:

$$F_{S,\max S} = \alpha^* \left(\frac{d_L}{2}\right)^2 {}^*\pi^*\tau_{SG} \tag{2}$$

Where α is an empirically fitted scaling factor accounting for nugget rotation and joint stiffness effects. The shear strength τ_{SG} was derived from literature data for representative materials [19,53–56] and fitted using a modified Hill function:

$$\tau_{SG}(R_m) = a - \frac{a}{1 + \left(\frac{R_m}{b}\right)^c} \tag{3}$$

The parameters a, b, and c are empirically fitted constants. R_m is the ultimate tensile strength of the respective sheet material, and for dissimilar joints, the FZ strength was computed as a thickness-weighted average of the base materials. Fig. 17 (a) shows the correlation between tensile and shear strength, while Fig. 17 (b) visualizes the predicted maximum load depending on nugget diameter and tensile strength.

In the case of button pull-out, the effective load-bearing area was described as a ring around the nugget, with its strength governed by the tensile strength and ductility of the base material. The model captured both ductile and brittle button pull-out behavior and reproduced the experimentally observed stagnation in strength at high material strengths. For button pull-out, a rational function was used to capture the nonlinear relationship between tensile strength and energy absorption in the tearing process. The maximum force is modeled as:

$$F_{S,max\ P} = \frac{d_L}{2}{}^*\pi^* f(t)^* a - \frac{a}{1 + \left(\frac{R_m}{b}\right)^c}{}^* f\left(R_{m,dif}\right) \tag{4}$$

Where f(t) is a thickness-dependent correction factor derived from regression analysis. To represent the mismatch in mechanical properties, the function $f(R_{m,diff})$ was introduced. It captures the effect of strength asymmetry between joined sheets and is calculated as a normalized difference in tensile strength. This parameter varies depending on the loading condition. Here, t_1, t_2, and t_3 denote the sheet thicknesses. For outer-to-outer (T–B) loading, the difference is computed as:

$$R_{m,dif\ O-U} = \frac{t_1}{t_1 + t_2}{}^* R_{m1} - \frac{t_2}{t_1 + t_2}{}^* R_{m2} \tag{5}$$

For asymmetric 3-LJ loading configurations such as T–M or M–B, the passive outer sheet also contributes to joint stiffness and must be included:

$$R_{m,dif\ O-M,M-U} = \frac{t_1}{t_1 + t_2 + t_3}{}^* R_{m1} - \frac{t_2 + t_3}{t_1 + t_2 + t_3}{}^* \frac{(R_{m2} + R_{m3})}{2} \tag{6}$$

Here, O—U, O-M, and M-U denote the load paths outer-to-upper, outer-to-middle, and middle-to-upper sheet, respectively. These effects are visualized in Fig. 18, which shows (a) the correlation between tensile and button pull-out strength, and (b) the predicted maximum force as a function of nugget diameter and tensile strength.

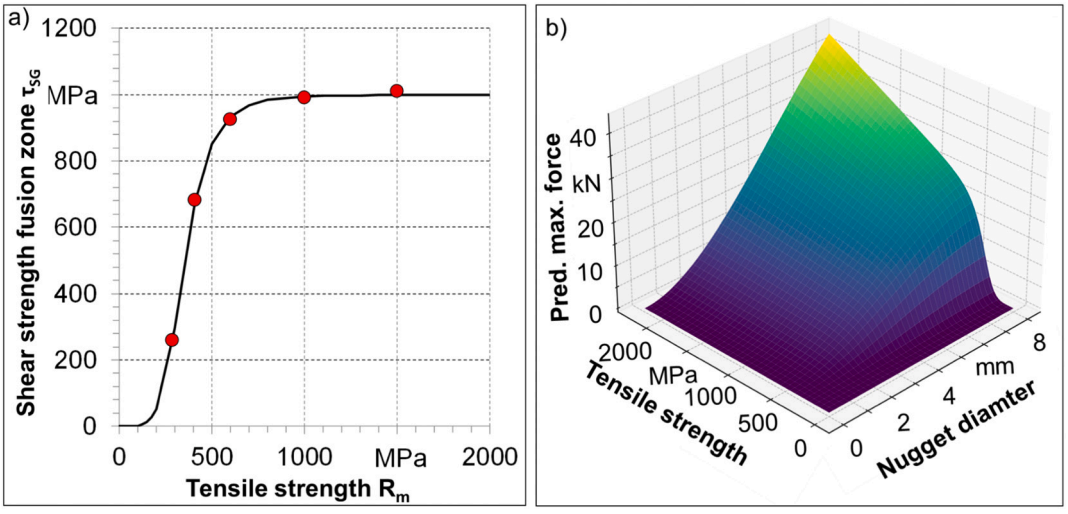

Fig. 17. a) Correlation between tensile and shear strength; b) Predicted maximum force as a function of nugget diameter and tensile strength for shear fracture.

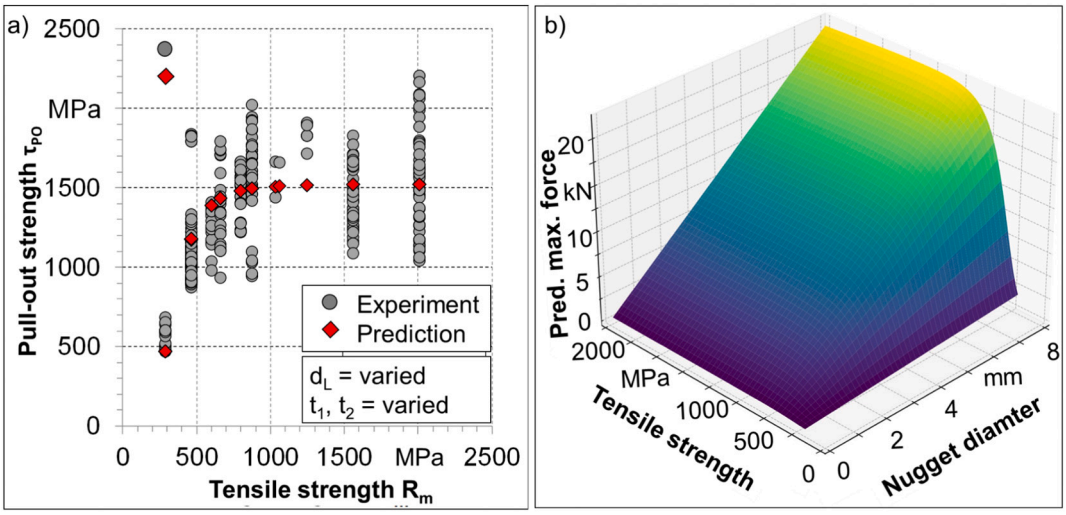

Fig. 18. a) Correlation between tensile and button pull-out strength; b) Predicted maximum force as a function of nugget diameter and tensile strength for button pull-out fracture.

To model tear-out failure, the maximum force was calculated as:

$$F_{S,max\ T} = a^{*}\frac{d_L}{2}{}^{*}\pi^{*}t^{*}\frac{b^{*}{R_m}^{c}}{d^{c}+{R_m}^{c}} \tag{7}$$

The parameters a, b, c, and d are empirically fitted constants. Tear-out is typically observed in 3-LJ when the middle sheet is weakest. The model accounts for this by evaluating all possible failure paths (O—U, O–M, M–U) and selecting the predicted maximum load in accordance with the minimum principle (Fig. 19).

A separate formulation was introduced for tensile and peel loading, which exhibit comparable fracture mechanisms dominated by button pull-out. While the same functional form was retained, the parameter sets were individually calibrated for each loading scenario:

$$F_{N,max} = a^{*}\left(\frac{d_L}{2}{}^{*}\pi^{*}t\right)^{b}{}^{*}\frac{c^{*}R_m}{d+e^{*}{R_m}^{2}}{}^{*}f\left(R_{m\ dif}\right) \tag{8}$$

Here, a, b, c, d, and e are empirically fitted constants. Under peel loading, failure is primarily governed by the same mechanisms observed under tensile loading, namely, localized plastic deformation and button pull-out. As such, the same functional formulation used for tensile failure (Eq. 7) was adopted to describe the load-bearing capacity under peel conditions. However, the model parameters were recalibrated to reflect the specific force levels and failure characteristics observed under peel loading. Fig. 20 shows the predicted maximum force as a function of nugget diameter and tensile strength for tensile and peel loading.

Under tensile loading, some joints exhibited simultaneous button pull-out failure in the middle and passive outer sheet. In such cases, the predicted maximum load was calculated as the sum of both button pull-out capacities. This combined mechanism is illustrated in Fig. 21.

The formulations in Eqs. 2–8 were derived and calibrated using welds produced with optimized process parameters, ensuring that common defects such as dome failure were suppressed. Under these conditions, the strength of the base material and the HAZ is implicitly accounted for through the dependence on the ultimate tensile strength (R_m). As a result, the model naturally reproduces experimentally observed trends, such as the stagnation of load-bearing capacity under

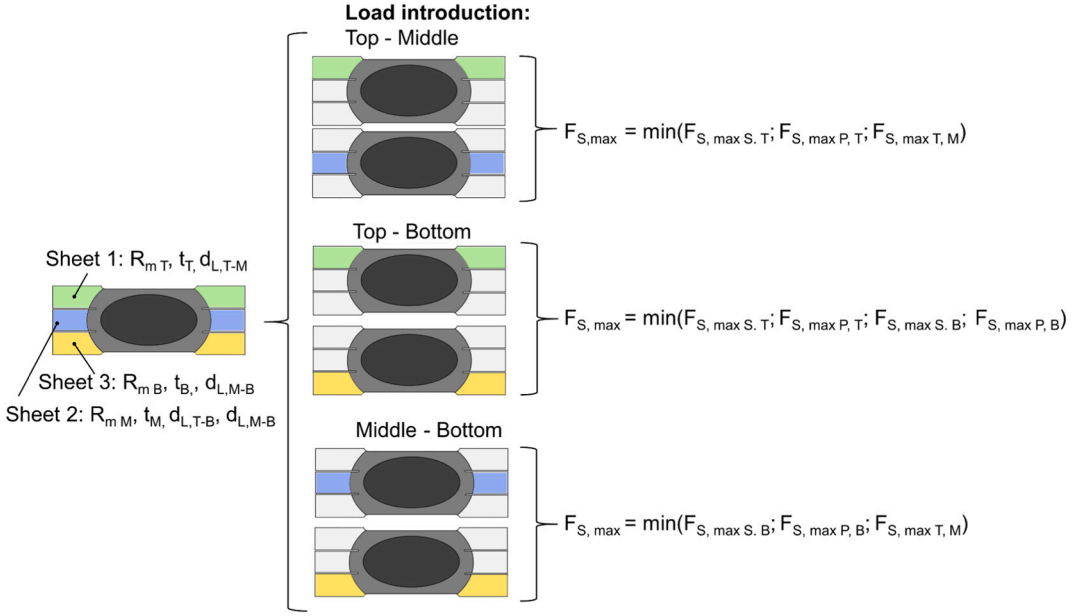

Fig. 19. Illustration of the calculation procedure for determining the maximum load of a three-layered joint under shear loading.

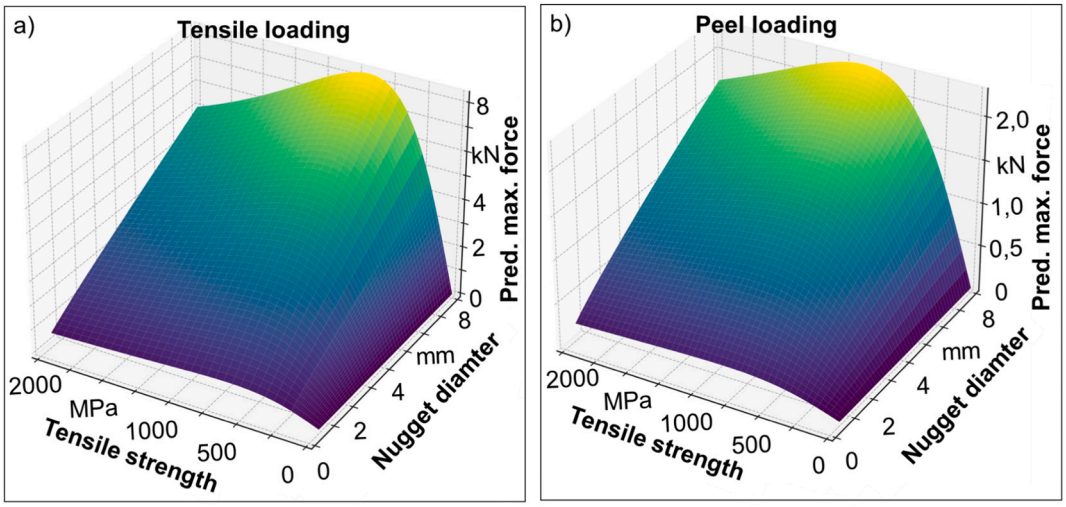

Fig. 20. Predicted maximum force as a function of nugget diameter and tensile strength for (a) tensile loading and (b) peel loading.

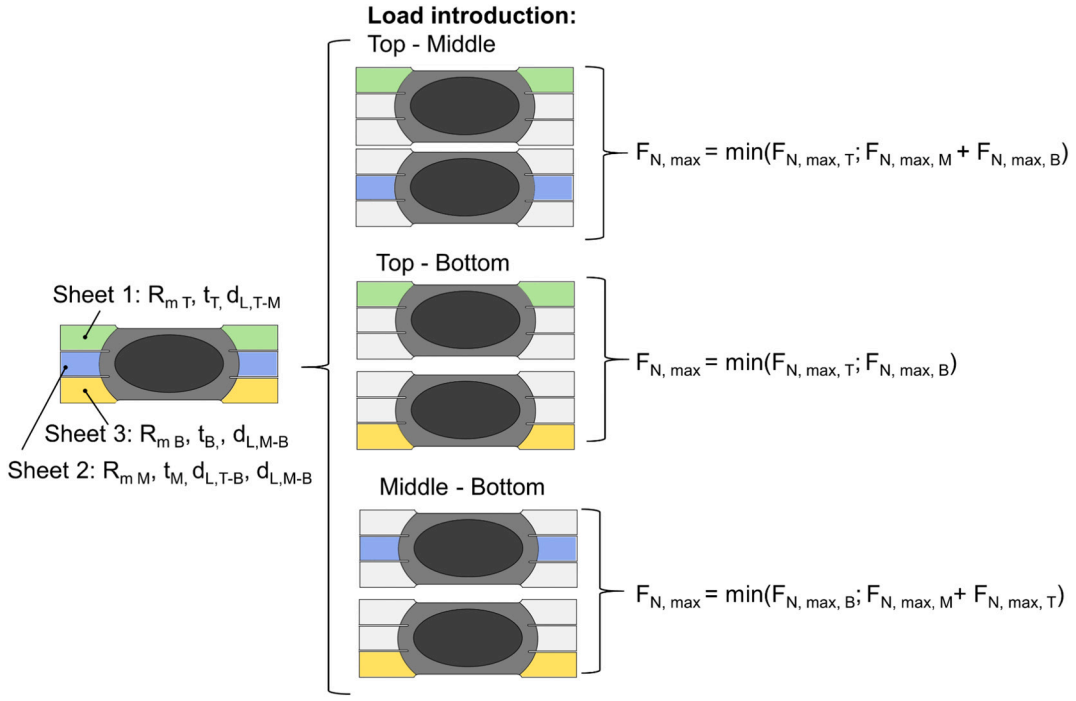

Fig. 21. Illustration of the calculation procedure for determining the maximum load of a three-layered joint under tensile loading.

shear loading and its decrease beyond a maximum under tensile loading. These effects reflect the combined influence of hardness gradients, HAZ softening, and local microstructural variations. Additional statistical analyses tested whether including explicit parameters such as local hardness minima, maxima, or HAZ width would further improve prediction accuracy. However, no significant improvement was observed, and such terms were therefore not included to preserve robustness and transferability of the prediction method.

To ensure robustness, the model parameters were optimized using an evolutionary strategy [49,50], as described in Section 2. The optimization refined the parameter sets for each failure mode and significantly improved the fit for button pull-out and tear-out failures. The RMSE was reduced by up to 20 % while maintaining physical interpretability of the model equations.

3.6. *Discussion and validation of the prediction model*

The prediction formulas presented in this study quantitatively incorporate parameters such as nugget diameter, sheet thickness, and tensile strength, which were identified in Sections 3.1–3.3 as the primary drivers of joint capacity. Stiffness effects were integrated through the thickness-to-strength ratio, reflecting their role in constraining nugget rotation. Other findings, including the stacking sequence of materials, the application of the minimum rule, and the occurrence of secondary failure mechanisms, were not included directly in the analytical equations but were systematically implemented in the calculation procedure. These principles determine which equation is applied under a given configuration and how the predicted failure mode is assigned, thereby ensuring that the model reflects both quantitative correlations and mechanistic insights derived from the experiments and simulations.

The developed method demonstrated high agreement with experimental data across all loading conditions. Model performance metrics were evaluated on an independent test set not used during training. In shear loading scenarios, the model achieved a coefficient of determination (R^2) of 88.8 %, reflecting its strong predictive capability. For tensile loading, the model attained an R^2 of 78.6 %, while for peel loading, a satisfactory R^2 of 72.0 % was observed. Corresponding root mean square errors (RMSE) were between 1.34 kN and 1.94 kN for shear fracture, depending on the failure mode, 0.94 kN for tensile loading, and 0.357 kN for peel loading. Notably, the lower absolute force levels observed under peel loading contributed to relatively lower R^2 values, despite the low absolute RMSE. Due to the limited number of independent validation cases, confidence intervals were not reported. However, the consistency of RMSE and R^2 across all loading scenarios indicates the robustness of the developed methodology.

The final model showed excellent agreement with additional validation data, including material combinations not used during development. In the case of a 3-LJ using MnB1900 ($R_m = 2220$ MPa), the model predicted the maximum load with an RMSE of 0.965 kN, thereby outperforming the reference methods [16,20,23–25,57], as illustrated in Fig. 22.

The derived formulas not only provide accurate predictions of load-bearing capacity but also carry direct engineering significance. Their closed-form structure enables the development of design tools that facilitate the rapid and straightforward assessment of joint strength across various loading configurations. Such tools can be applied, for instance, to identify the optimal stacking sequence of sheets in three-layer joints or to estimate load-bearing capacities during the early design stages of automotive structures. To demonstrate this transfer into engineering practice, the formulas were implemented in a user-friendly software tool, available both as an Excel-based calculation sheet and as a web-based application. This tool requires only a limited set of input parameters, including sheet thicknesses, tensile strengths, nugget diameters, and loading configurations, and returns the predicted maximum load along with the expected failure mode. As such, it provides a fast and transparent means for comparing different joint configurations, supporting decision-making in material selection and structural design.

Beyond such stand-alone applications, the formulas could also be integrated into surrogate models for crash simulations or multi-scale analyses, thereby linking detailed joint-level predictions with full-vehicle performance assessments. This highlights the potential of the proposed approach to support both early-phase design decisions and advanced structural simulations in the automotive industry.

Compared to existing empirical regression models, the proposed method represents a significant advance by systematically integrating physically interpretable parameters into closed-form prediction formulas. This ensures not only high predictive accuracy but also mechanistic transparency, allowing the model to capture effects such as HAZ softening, nugget rotation constraints, and the influence of stacking sequence. To the best of the authors' knowledge, this is the first approach that provides a unified and transferable framework for predicting both the load-bearing capacity and the failure mode of three-layer RSW joints across a wide range of materials and loading configurations.

4. Conclusion

This study investigated the mechanical behavior and failure mechanisms of resistance spot-welded two-layer and three-layer joints (2-LJ and 3-LJ) using a combined approach of experimental testing, numerical simulations, and analytical modeling. A total of 19 joint configurations with varying material combinations, sheet thicknesses, and load introduction paths were examined to systematically analyze load-bearing behavior under shear, tensile, and peel loading. The main findings are summarized as follows:

(1) The Equivalent Similar Joint Strength (ESJS) has been introduced as a material-specific benchmark to predict fracture locations in dissimilar joints based on load orientation.
(2) The minimum principle was extended to 3-LJ, considering load path, stacking sequence, and deformation asymmetry. Failure typically occurred in the outer loaded sheet with lower ESJS but could shift to the middle or passive sheet under specific conditions.
(3) A physics-informed model was developed to predict maximum load and failure mode. Distinct equations were derived for interfacial fracture, button pull-out, and tear-out using nugget diameter, sheet thickness, and tensile strength as inputs. Failure mode transitions were captured via an extended minimum rule.
(4) The model showed strong predictive accuracy with R^2 values of 88.8 % (shear), 78.6 % (tensile), and 72.0 % (peel), and corresponding RMSEs of 1.34–1.94 kN, 0.94 kN, and 0.357 kN. Validation with ultra-high-strength steels confirmed robustness.

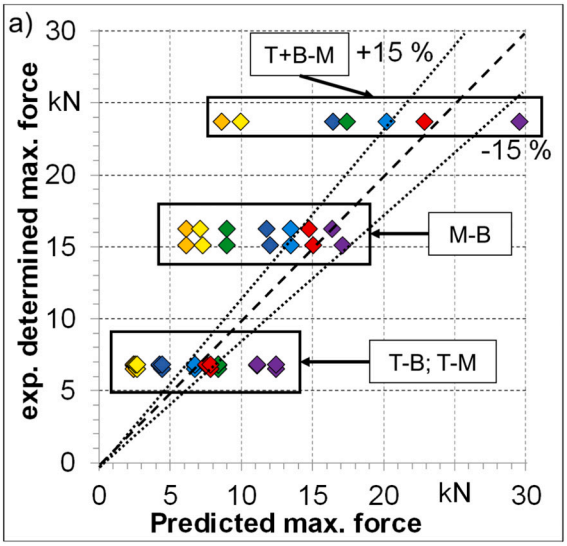

b)	Prediction method	RMSE
◆	Optimized model	0,9649 kN
◆	ISO 14373:2015 [44]	3,8581 kN
◆	AWS D8.1M [24]	8,3034 kN
◆	Varbai et al. [23]	4,4799 kN
◆	Májlinger et al. [25]	1,7903 kN
◆	Vijayan et al. [16]	4,5033 kN
◆	Cho et al. [20]	7,5682 kN

Fig. 22. a) Predicted versus experimentally determined maximum forces for a three-sheet joint compared across different models; b) RMSE values as a measure of predictive accuracy.

The novelty of this work lies in the establishment of a generalizable and physics-informed framework for three-layer spot welds, which goes beyond existing empirical models. By combining experimental insights with analytical modeling, the study demonstrates how local microstructural effects (e.g., HAZ softening, asymmetry in load transfer) can be translated into closed-form predictive equations. This provides both a deeper scientific understanding of multi-layer weld failure mechanisms and an engineering-relevant tool for early-stage design and digital engineering workflows. Building on this contribution, this work establishes a robust and transferable foundation for predicting the mechanical behavior of multi-layered resistance spot-welded joints. Beyond its immediate applicability in lightweight automotive design, the proposed framework provides a basis for integrating weld quality prediction into digital engineering workflows. Future research will focus on extending the model to dynamic and crash-relevant loading conditions, expanding its applicability to a wider range of advanced high-strength materials, and embedding the methodology into CAE environments for automated weld performance evaluation in early-stage vehicle development.

CRediT authorship contribution statement

Viktoria Olfert: Writing – review & editing, Writing – original draft, Validation, Project administration, Methodology, Investigation, Formal analysis, Data curation, Conceptualization. **Philipp Bähr:** Writing – review & editing, Formal analysis. **Lilia Schuster:** Writing – review & editing, Methodology, Formal analysis, Conceptualization. **Julia Westhoff:** Software, Data curation. **Keke Yang:** Writing – review & editing, Writing – original draft. **Enes Ibeski:** Software. **David Hein:** Writing – review & editing. **Silke Sommer:** Supervision, Funding acquisition. **Gerson Meschut:** Supervision, Funding acquisition.

Declaration of competing interest

The authors declare that they have no known competing financial interests or personal relationships that could have appeared to influence the work reported in this paper.

Acknowledgments

The research project IFG 20998 N / P 1431 “Development of methods for predicting the crash behavior of resistance spot-welded 3-steel sheet joints” from the Research Association for Steel Application (FOSTA), Düsseldorf, is supported by the Federal Ministry for Economic Affairs and Climate Action through the German Federation of Industrial Research Associations (AiF) under the Industrial Collective Research (IGF) programme on the basis of a decision by the German Bundestag. The project is carried out at LWF, Paderborn University, and Fraunhofer IWM.

References

[1] Wang Y, Hao Y, Hou Y, Quan Q, Li Y. Optimizing scope 3 emissions in the automotive manufacturing industry: a multidisciplinary approach. Carbon Res 2024:3. https://doi.org/10.1007/s44246-024-00131-2.
[2] Braess HH, Seiffert U. Vieweg Handbuch Kraftfahrzeugtechnik. Wiesbaden: Springer Fachmedien Wiesbaden; 2013.
[3] Klein B, Gänsicke T. Leichtbau-Konstruktion. Wiesbaden: Springer Fachmedien Wiesbaden; 2019.
[4] Hickey K. What makes 3rd generation AHSS grades so unique? [Online]. Available: https://worldsteel.org/media-centre/blog/2021/3rd-generation-ahss-grades-unique/ (accessed: Jul. 15 2025).
[5] Hinton-Beales D. Car manufacturers look to steel for stronger, lighter cars. [Online]. Available: https://worldsteel.org/steel-stories/automotive/manufacturers-stronger-lighter-cars-ahss/ (accessed: Jul. 15 2025).
[6] Zhou K, Yao P. Overview of recent advances of process analysis and quality control in resistance spot welding. Mech Syst Signal Process 2019;124:170–98. https://doi.org/10.1016/j.ymssp.2019.01.041.
[7] Ziegler A, Heidling E. The Chip crisis in the automotive industry. München: HyValue; 2023. https://doi.org/10.36194/HyValue_Chip_Crisis_2023.
[8] Ryberg AB, Nilsson L. Spot weld reduction methods for automotive structures. Struct Multidiscip Optim 2016;53:923–34. https://doi.org/10.1007/s00158-015-1355-4.
[9] Williams NT, Parker JD. Review of resistance spot welding of steel sheets part 1 modelling and control of weld nugget formation. Int Mater Rev 2004;49:45–75. https://doi.org/10.1179/095066004225010523.
[10] Brechelt S, Neef P, Wiche H, Wesling V. Spot weld bonding – process behavior of three-sheet steel stack ups and analysis strategies with online measuring methods. Manuf Rev 2020;7:3. https://doi.org/10.1051/mfreview/2019029.
[11] Sommer S, Steffes-lai D, Clees T. Consideration of process-related variations of spot welded joints. ATZelectronics worldwide 2013;115:44–9. https://doi.org/10.1007/s38311-013-0143-2.
[12] Zhou L, et al. Comparative study on resistance and displacement based adaptive output tracking control strategies for resistance spot welding. J Manuf Process 2021;63:98–108. https://doi.org/10.1016/j.jmapro.2020.03.061.
[13] Chebbi T, Tlili B, Bouzaiene H, Guizani H, Chafra M. Failure mode prediction of resistance spot welded quenching and partitioning stainless steel. J Braz Soc Mech Sci Eng 2021:43. https://doi.org/10.1007/s40430-021-03218-8.
[14] Boriwal L, Sarviya RM, Mahapatra MM. Process analysis and regression modelling of resistance spot welded joints of austenitic stainless steel 304L and low carbon steel sheets by using surface response methodology. Proc Inst Mech Eng Part E J Process Mech Eng 2021;235:24–33. https://doi.org/10.1177/0954408920940888.
[15] Rajalingam P, Rajakumar S, Balasubramanian V, Sonar T, Kavitha S. Tensile shear fracture load bearing capability, softening of HAZ and microstructural characteristics of resistance spot welded DP-1000 steel joints. Mater Test 2023;65:94–110. https://doi.org/10.1515/mt-2022-0236.
[16] Vijayan V, Murugan S, Son S, Park YD. Shrinkage void formation in resistance spot welds: its effect on advanced high-strength-steel weld strength and failure modes. J Mater Eng Perform 2019;28:7514–26. https://doi.org/10.1007/s11665-019-04465-6.
[17] Dorribo D. Development of mechanism-based models for resistance spot weld failure simulation of multi-material advanced high strength steel sheets. PhD thesis. Universitat Politecnica de Catalunya 2018.
[18] Pouranvari M, Marashi SPH. Failure behavior of three-steel sheets resistance spot welds: effect of joint design. J Mater Eng Perform 2012;21:1669–75. https://doi.org/10.1007/s11665-011-0078-y.
[19] Schuster L, Sommer S. Charakterisierung und Meta-Modellierung von ungleichartigen Punktschweißverbindungen für die Crashsimulation. Freiburg AVIF A 2020;294.
[20] Cho H, Nam S, Kang M, Kim Y. Predicting failure modes of resistance spot welds from the chemical composition of materials. J Weld Join 2020;38:450–9. https://doi.org/10.5781/JWJ.2020.38.5.4.
[21] Brandhuber M. Verbesserung der Prognosegüte des Versagens von Punktschweißverbindungen bei höchstfesten Stahlgüten. Bamberg: Meisenbach; 2012.
[22] Huin T, Dancette S, Fabrègue D, Dupuy T. Investigation of the failure of advanced high strength steels heterogeneous spot welds. Metals 2016;6:111. https://doi.org/10.3390/met6050111.
[23] Varbai B, Sommer C, Szabó M, Tóth T, Májlinger K. Shear tension strength of resistant spot welded ultra high strength steels. Thin-Walled Struct 2019;142:64–73. https://doi.org/10.1016/j.tws.2019.04.051.
[24] Specification for automotive weld quality resistance spot welding of steel, AWS D8.1M. American Welding Society; 2021.
[25] Májlinger K, Katula L, Varbai B. Prediction of the shear tension strength of resistance spot welded thin steel sheets from high- to ultrahigh strength range. Period Polytech Mech Eng 2021;66:67–82. https://doi.org/10.3311/PPme.18934.
[26] Pouranvari M, Marashi SPH. Weld nugget formation and mechanical properties of three-sheet resistance spot welded low carbon steel. Can Metall Q 2012;51:105–10. https://doi.org/10.1179/1879139511Y.0000000028.
[27] Mao X, Cheng Z, Zhu Q, Wang W, Wei X, Zhao Y. Effect of different lapping orders on mechanical performance and nugget forming process for three-sheet dissimilar resistance spot welding joints between DC06 and unequal-thickness hot-stamped B1500HS steel sheets. Metall Res Technol 2021;118:112. https://doi.org/10.1051/metal/2020094.
[28] Mikno Z, Grzesik B, Stępień M. The investigation on the ideal spot weld numerical model in resistance welding. Int J Adv Manuf Technol 2020;111:895–907. https://doi.org/10.1007/s00170-020-06114-y.
[29] Nielsen KL. 3D modelling of plug failure in resistance spot welded shear-lab specimens (DP600-steel). Int J Fract 2008;153:125–39. https://doi.org/10.1007/s10704-008-9305-4.
[30] Chung K, Noh W, Yang X, Han HN, Lee MG. Practical failure analysis of resistance spot welded advanced high-strength steel sheets. Int J Plast 2017;94:122–47. https://doi.org/10.1016/j.ijplas.2016.10.010.
[31] Sadasue T, Igi S, Taniguchi K, Ikeda R, Oi K. Fracture behaviour and numerical study of resistance spot welded joints in high-strength steel sheet. Weld Int 2016;30:602–13. https://doi.org/10.1080/09507116.2016.1142187.
[32] Ma Y, et al. Measurement of local material properties and failure analysis of resistance spot welds of advanced high-strength steel sheets. Mater Des 2021;201:109505. https://doi.org/10.1016/j.matdes.2021.109505.
[33] Su Y, Song K, Hu Z, Chen J, Du Z. Numerical simulation and experimental investigation of resistance spot welding with initial gap under tensile shear load. J Manuf Process 2024;124:1102–11. https://doi.org/10.1016/j.jmapro.2024.07.027.
[34] Lv TL, et al. Multi-physical process simulation of resistance spot welding available for synthetic data generation. J Manuf Process 2025;141:709–24. https://doi.org/10.1016/j.jmapro.2025.03.024.

[35] Chtourou R, Leconte N, Chaari F, Haugou G, Markiewicz É, Zouari B. Macro-modeling of the strength and failure of multi-layer multi-steel grade spot welds: connector formulation, assembly model and identification procedure. Thin-Walled Struct 2017;113:228–39. https://doi.org/10.1016/j.tws.2017.01.023.
[36] Khan Q, Ghassemi-Armaki H, Gill A, Zillicink S, Gawade A. Characterization and modeling of spot-weld joints with *MAT_100_DA parameter optimization using LS-OPT ® and 3 sheet spot-weld modeling method development in LS-DYNA®. 2018.
[37] Xia YJ, Song Q, Yi B, Lyu T, Sun Z, Li Y. Improving out-of-distribution generalization for online weld expulsion inspection using physics-informed neural networks. Weld World 2025;69:1309–22. https://doi.org/10.1007/s40194-025-01950-6.
[38] DIN EN ISO 18278-2: Widerstandsschweißen - Schweißeignung - Teil 2: Verfahren zum Bewerten der Eignung für das Widerstandspunktschweißen, 18278–2:2016, DIN Deutsches Institut für Normung e.V.; 2016.
[39] Ermittlung mechanischer Eigenschaften an Blechwerkstoffen bei hohen Dehnraten im Hochgeschwindigkeitsdehnversuch SEP 1230:2007–02, 1230:2007–02, Verbands der deutschen Automobilindustrie (VDA) und des Stahlinstituts VDEh; 2007.
[40] Sherepenko O, Kazemi O, Rosemann P, Wilke M, Halle T, Jüttner S. Transient softening at the fusion boundary of resistance spot welds: a phase field simulation and experimental investigations for Al–Si-coated 22MnB5. Metals 2020;10:10. https://doi.org/10.3390/met10010010.
[41] Cretteur L, Merdji Y, Kaczynski C. Spot weld strength improvement by optimization of the welding parameters on 1.8 GPa Press Hardened Steels. In: CHS2-series, no. 7, 7th International Conference Hot Sheet Metal Forming of High-Performance Steel, June 2-5. Luleå, Sweden. 1st ed. Auerbach/Vogtl: Verlag Wissenschaftliche Scripten; 2019. p. 2019.
[42] Kerl H. Ein Beitrag zur Standmengenerhöhung der Elektrodenkappen beim Widerstandspunktschweißen. Dissertation: Technische Universität Clausthal, Clausthal; 2018.
[43] Ramachandran DC, Figueredo B, Sherepenko O, Jin W, Park YD, Biro E. A study on improving the mechanical performance by controlling the halo ring in the Q&P 980 steel resistance spot welds. J Manuf Process 2022;75:320–30. https://doi.org/10.1016/j.jmapro.2022.01.019.
[44] Burget S. Modellierung des Verformungs- und Versagensverhaltens punktgeschweißter Mischverbindungen zwischen mikrolegierten und pressgehärteten Stählen. 2016.
[45] Hahn O, Rohde A, Gieske D. Verfahren zur Herstellung von Proben und Probenspannvorrichtung. Nr. 195 22 247, München.
[46] von Schweißpunkten Prüfung. Merkblatt, DVS 2916. Düsseldorf: Deutscher Verband für Schweißtechnik e.V; 1978.
[47] Schuster L, et al. Influences of weld nugget shape and material gradient on the shear strength of resistance spot-welded joints. Steel Res Int 2024. https://doi.org/10.1002/srin.202300530.
[48] Nielsen CV, Zhang W, Perret W, af Martins P, Bay N.. Three-dimensional simulations of resistance spot welding. Proc Inst Mech Eng Part D J Automob Eng 2015;229:885–97. https://doi.org/10.1177/0954407014548740.
[49] Evolutionäre Hollstein R, Algorithmen.. In: Optimierungsmethoden. Wiesbaden: Springer Fachmedien Wiesbaden; 2023. p. 147–84.
[50] Divis Intelligent Solutions GmbH. The CVA Python Package. [Online]. Available: https://divis-gmbh.de/cva4py_doc/overview.html (accessed: Jul. 31 2025).
[51] Tamizi M, Pouranvari M, Movahedi M. The role of HAZ softening on cross-tension mechanical performance of martensitic advanced high strength steel resistance spot welds. Metall Mater Trans A 2021;52:655–67. https://doi.org/10.1007/s11661-020-06104-5.
[52] Olfert V, Schuster L, Bähr P, Hein D, Meschut G, Sommer S. Methodenentwicklung zur Prognose des Crashverhaltens von widerstandspunktgeschweißten 3-Stahl-blechverbindungen (WPS-Crash 3-Blech). IGF-Projekt Nr. 20998 N / P 1431; 2023.
[53] Gumbsch P, Sommer S, Burget S. Roos E. Krätschmer D. Charakterisierung Und Ersatzmodellierung Des Bruchverhaltens von Punktschweißverbindungen Aus Ultrahochfesten Stählen Für Die Crashsimulation Unter Berücksichtigung Der Auswirkung Der Verbindung Auf Das Bauteilverhalten: Wink HJ; 2012.
[54] Sommer S, Burget S, Bentele R. Bruchverhalten von hochfesten Stählen beim Widerstandspunktschweißen – Schädigungssimulation. IWM Bericht V1134/2014, K-Projekt Join4+; 2014.
[55] Sommer S, et al. Charakterisierung und Modellierung der Beeinflussung des Bauteilverhaltens durch Erweichungszonen an Schweißpunkten höchst- und ultrahochfester Stähle unter Crashbelastung. In: Düsseldorf: Forschungsvereinigung Stahlanwendung e.V. FOSTA; 2019.
[56] Sommer S, Sun D. Charakterisierung und Bewertung der Tragfähigkeit punktgeschweißter Stahlblechverbindungen unter Crashbelastung mit Hilfe von erweiterten Schädigungsmodellen. AVIF-Forschungsvorhaben 2006;Nr. A 173 / S24/10055/03.
[57] Widerstandsschweißen – Verfahren zum Punktschweißen von niedriglegierten Stählen mit oder ohne metallischem Überzug, 14373:2015, DIN Deutsches Institut für Normung e.V., Berlin; 2015.